

O-glycans Expand Lubricin and Attenuate Its Viscosity and Shear Thinning

Saber Boushehri, Hannes Holey, Matthias Brosz, Peter Gumbsch, Lars Pastewka, Camilo Aponte-Santamaría,* and Frauke Gräter*



Cite This: <https://doi.org/10.1021/acs.biomac.3c01348>



Read Online

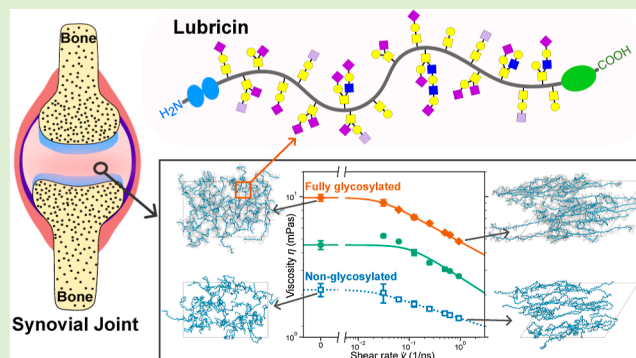
ACCESS |

Metrics & More

Article Recommendations

Supporting Information

ABSTRACT: Lubricin, an intrinsically disordered glycoprotein, plays a pivotal role in facilitating smooth movement and ensuring the enduring functionality of synovial joints. The central domain of this protein serves as a source of this excellent lubrication and is characterized by its highly glycosylated, negatively charged, and disordered structure. However, the influence of O-glycans on the viscosity of lubricin remains unclear. In this study, we employ molecular dynamics simulations in the absence and presence of shear, along with continuum simulations, to elucidate the intricate interplay between O-glycans and lubricin and the impact of O-glycans on lubricin's conformational properties and viscosity. We found the presence of O-glycans to induce a more extended conformation in fragments of the disordered region of lubricin. These O-glycans contribute to a reduction in solution viscosity but at the same time weaken shear thinning at high shear rates, compared to nonglycosylated systems with the same density. This effect is attributed to the steric and electrostatic repulsion between the fragments, which prevents their conglomeration and structuring. Our computational study yields a mechanistic mechanism underlying previous experimental observations of lubricin and paves the way to a more rational understanding of its function in the synovial fluid.



INTRODUCTION

Friction and adhesion involving viscous fluids or viscoelastic materials, such as those occurring in adhesives or lubricants, significantly impact various aspects of everyday life, from human interaction with the environment to the performance and reliability of machinery. Synovial joints, including the knee, hip, and shoulder, are essential for facilitating the smooth movements of the human body. These joints exhibit remarkable lubricating properties, characterized by an extremely low coefficient of friction (ranging from 0.0005 to 0.04) and the ability to withstand pressures of approximately 200 atm (Figure 1A). Lubricin, a mucinous glycoprotein that contains an intrinsically disordered region, plays a crucial role in providing excellent lubrication by reducing friction within synovial joints. In the case of synovial joints, the viscoelastic response of lubricin at the molecular level gives rise to efficient tissue lubrication, enabling it to withstand high mechanical loads at the macroscopic scale.^{1–5} However, the determining factors of lubricin's molecular structure and dynamics underlying its lubricating function remain to be understood.

Lubricin is encoded by the PRG4 (proteoglycan 4) gene. It is composed of approximately 1400 amino acids and has a length of approximately 200 nm ± 50 nm.⁶ Structurally, lubricin comprises two folded terminal domains, referred to as

the N and C terminal domains, which are predominantly nonglycosylated, positively charged, and hydrophobic. These terminal domains enable lubricin to anchor to cartilage proteins, contributing to its ability to adsorb and withstand pressure.^{7–9} In contrast, the central domain of lubricin has been referred to be structureless, or in other words intrinsically disordered,^{6,7,10} a structural feature corroborated by AlphaFold¹¹ and the intrinsic disorder predictor PrDOS¹² (Figure S1). This region is known as the mucin-like domain and is highly glycosylated, negatively charged and therefore highly hydrophilic.^{10,13} Approximately 30–35% of the overall lubricin structure is composed of core I and core II O-linked glycans, namely, sugar molecules attached to the hydroxyl group of serine (Ser) or threonine (Thr) residues. These O-glycans, along with sialic acid, contribute to negative charges in the protein^{14–16} (Figure 1B,C). The mucin-like domain is very rich in prolines too.¹³

Received: December 7, 2023

Revised: April 26, 2024

Accepted: April 26, 2024

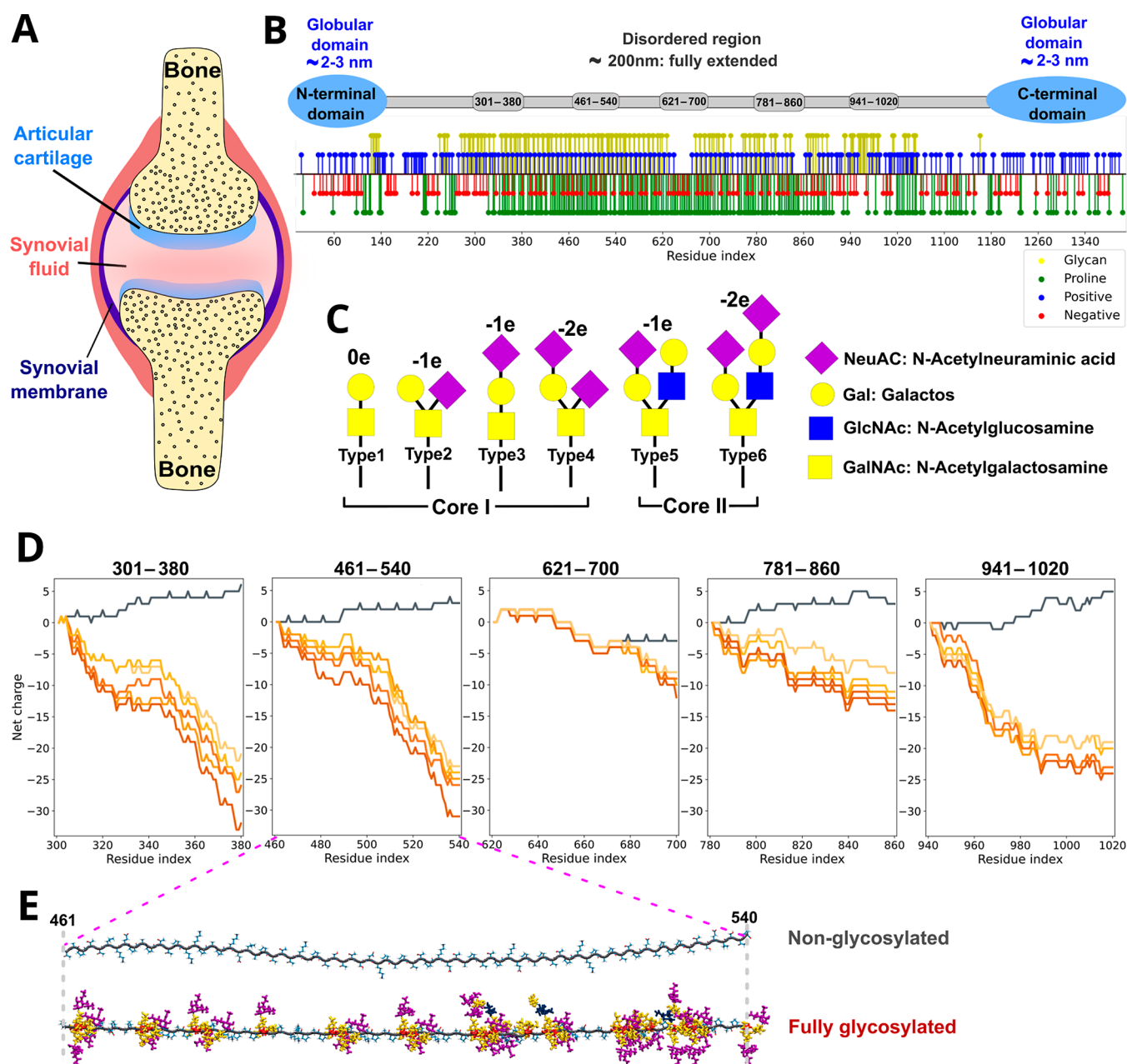


Figure 1. Sequence, charge, and glycosylation of lubricin. (A) Schematic representation of the human synovial joint. Lubricin is found in the synovial fluid and acts as a lubricant to ensure the smooth movement of bones. (B) Lubricin is composed of two globular terminal domains (blue) and a mucin-like central disordered region (gray). The two globular domains are nonglycosylated. The central region spans approximately 800 amino acids, is highly glycosylated by negatively charged O-glycans, and is rich in polar and proline residues. Glycan sites, charged residues, and proline residues along the sequence are indicated. (C) Core I and core II of six O-glycans of lubricin (out of 11 types) used in this study. The NeuAC sugar has a negative charge (purple diamond). The net charge of each type of O-glycan and the prevalence for lubricin are indicated. (D) Five different 80-amino acid fragments spanning the disordered region of lubricin. They were glycosylated to a different extent (six levels of glycosylation for each fragment). The cumulative net charge for each glycosylated fragment is shown. (E) Examples of the initial fully extended structure for a nonglycosylated and a fully glycosylated fragment (sequence 461–540).

The lubricating properties of lubricin are believed to be closely tied to its structural characteristics, with its high extent of glycosylation and disorder likely playing a vital role.^{17,18} However, the specific effects of glycosylation and disorder on the structure and viscosity of lubricin have yet to be fully elucidated. Specifically, glycosylation has been observed to play a key role on the lubrication of mucins^{19–22} and on the mechanical response of aggrecan.²³ It is reasonable to think that it may also affect the rheological properties of lubricin too.

The synovial fluid shows shear thinning,^{24–26} just as many other industrial or biological systems, from molecular inks and Nafion to cellulose hydrogels, mucus, and blood.^{27–30} Shear thinning is one of the most common types of non-Newtonian behavior observed in polymers, where the apparent viscosity of the solution decreases with increasing shear rates.³¹

Nonequilibrium molecular dynamics (NEMD) simulations have previously proven highly useful for studying the response of a polymer solution to shear at the molecular level. Shear rates can be induced across simulation systems by deforming

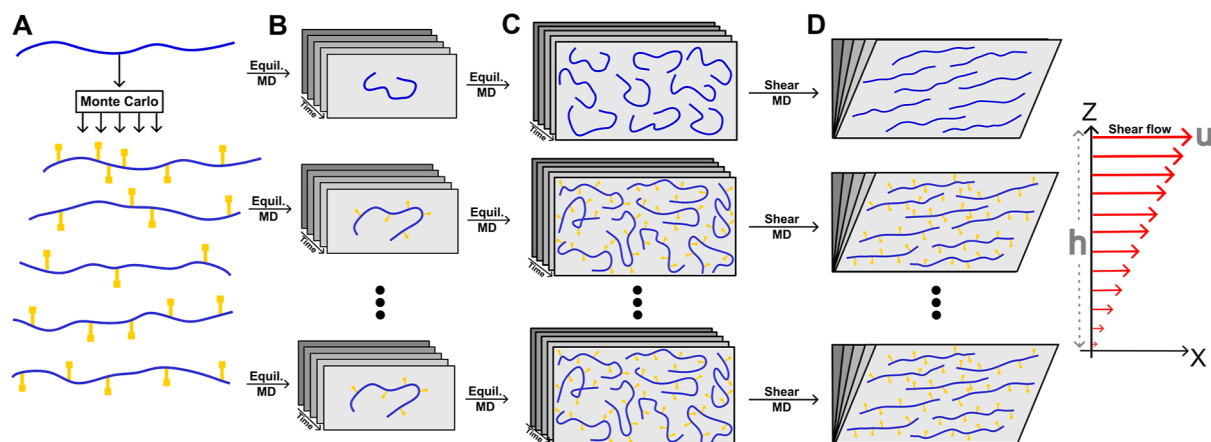


Figure 2. MD protocol to obtain viscosities of lubricin-derived fragments. (A) By using Monte Carlo sampling, we generated five different glycosylation distributions for each of the five 80-amino acid long lubricin fragments. Here, the blue line indicates the nonglycosylated fragment and the yellow symbols depict the O-glycans. (B) EMD simulations were carried out for each fragment, both in its nonglycosylated and its five different glycosylated forms. (C) EMD simulations were performed for systems containing multiple fragments in order to obtain the viscosity in the absence of shear by using the GK method. (D) Shear-driven NEMD simulation, deforming the simulation box, estimated viscosity under different shear rates.

the simulation box, using the so-called SLLOD algorithm,^{32,33} by dragging parallel walls relative to each other at a constant velocity,^{30,34,35} or also in combination with continuum models.^{36,37} Previous studies have successfully addressed the collapse propensities and intramolecular interactions of glycosylated disordered proteins by MD simulations at both atomistic^{38,39} and coarse-grained levels.⁴⁰ However, their behavior under shear, to the best of our knowledge, has not yet been explored.

In this study, we use a large set of equilibrium and shear-driven NEMD simulations (Figure 2) and continuum calculations to explore the molecular determinants of lubricin's function in reducing friction in synovial joints. Specifically, we aim to comprehensively understand how O-glycans impact lubricin-induced viscosity. We assess lubricin's zero shear viscosity and its shear viscosities under varying shear rates.^{30,41,42} Glycosylation expands lubricin in equilibrium and reduces its level of intermolecular clustering. Glycosylation leads to overall lower viscosities when the same mass densities are compared, but these viscosities drop less pronouncedly under shear. Additionally, to demonstrate the broad utility of our molecular viscosity and shear thinning analysis in a multiscale context, we conduct representative continuum simulations using fluid models guided by our MD data.^{43,44} By shedding light on the structural and rheological properties of glycosylated lubricin, this study enhances our understanding of synovial joints.

MATERIALS AND METHODS

Glycosylation of Lubricin Fragments. In order to investigate the effect of O-glycans on the structure of lubricin, we selected five distinct segments, each spanning 80 amino acids of the central disordered part of lubricin (Figure 1B). These segments represent the protein's physicochemical properties, including glycosylation, charged residues, and proline content. Consideration of ~80 amino acid fragments has been shown to be still computationally tractable.^{45,46} Moreover, taking into account multiple of such fragments along a long intrinsically disordered region has been proven useful to capture the key local properties of such a long disordered region.⁴⁶ Among the 11 types of oligosaccharides that bind to lubricin,¹⁵ we chose six types (depicted in Figure 1C) based on their composition and charge (more information in Figure S2). These six types of glycans were

attached to the hydroxyl groups of glycosylated serine/threonine (Ser/Thr) side chains, as defined by Ali et al.,¹³ within each lubricin segment. The exact level of binding of the O-glycan at each position is unknown. For this reason, we added glycans following five distinct oligosaccharide distributions based on a Monte Carlo sampling approach. In brief, we randomly added each type of glycan to the fragments based on the percentage (%) of total O-glycans (Figure S2B). By following this protocol, we generated one nonglycosylated and five different glycosylated versions of each lubricin fragment. The sugars that were attached at each glycosylation site in the 25 different cases are listed in Tables S1–S6, resulting in varying cumulative net-charge distributions (Figure 1D and Table S7).

We generated the initial structure of the nonglycosylated fragments by employing the Avogadro software package.⁴⁷ The addition of O-glycans was carried out by using the glycam.org server. Fully elongated linear configurations were considered in all cases.

Single-Chain EMD Simulations. MD simulations were performed using GROMACS (2020 version) software.⁴⁸ The amber99sb-star-ildnp^{49,50} force field was employed for the protein, and the GLYCAM06⁵¹ force field for carbohydrates. Force field parameters from GLYCAM06 were converted to GROMACS format using the ACPYPE script.^{52,53}

Initial structures were placed within a dodecahedron-shaped simulation box, solvated with TIP4P-D⁵⁴ water molecules and 150 mM NaCl ions. Additional ions were added to neutralize the net charge of the fragments (ranging from 6 chloride ions to counteract the most positive fragment to 3 sodium ions for the most negative one). The resulting systems had approximately 0.36–0.92 M atoms (see Table S8). The systems were subjected to energy minimization using a steepest descent algorithm until the maximum atomic force was below 1000 kJ mol⁻¹ nm⁻¹. The systems were thermalized in the NVT ensemble at a temperature of 310 K by using the velocity rescaling thermostat⁵⁵ during 1 ns (coupling time of 0.1 ps). Subsequently, the solvent was relaxed in the NPT ensemble at a pressure of 1 atm using the Parrinello–Rahman barostat⁵⁶ for 2 ns (coupling constant of 2.0 ps and reference compressibility of 4.5 × 10⁻⁵ bar⁻¹). In both equilibration parts, a harmonic force (with an elastic constant of 1000 kJ mol⁻²) was applied to restrain the position of the heavy atoms. Finally, production runs were executed under the NPT ensemble (same temperature and pressure as in equilibration steps) by applying periodic boundary conditions and releasing the position restraints on the heavy atoms (Figure 2B). The velocity rescale thermostat and the Parrinello–Rahman algorithm were employed in these to maintain a constant temperature and a constant

pressure during production runs too. Three replicas of 200 ns each were carried out for each of the 30 different fragments (Table S8).

Electrostatic interactions were taken into account by using the particle mesh Ewald algorithm.⁵⁷ Short-range interactions were modeled with a Lennard-Jones potential truncated at a cutoff distance of 1.0 nm. Bonds involving hydrogen atoms of the glycosylated fragments were constrained by using LINCS.⁵⁸ Accordingly, equations of motion were numerically integrated by using the Leapfrog algorithm at discrete time steps of 2 fs. Neighbors were treated with the Verlet buffer with a tolerance of 0.005 kJ mol⁻¹ ps⁻¹ and neighbors were updated every 10 steps.

Multichain EMD Simulations. To investigate the influence of lubricin glycosylation on medium viscosity, five distinct lubricin systems were considered, each with the same molar and mass density (30 nonglycosylated, 73 nonglycosylated, 101 nonglycosylated, 30 medium glycosylated, and 30 highly glycosylated chains) (Figure 2C). However, although the systems included 30 nonglycosylated (w.o. $\rho = 66.5$ kg/m³) and 30 highly glycosylated (w.+ $\rho = 230.6$ kg/m³) peptides matched in a molar concentration ($N = 30$), they had different mass densities. To establish the effect of glycosylation for constant mass density, a system comprising 101 nonglycosylated peptides was in addition introduced, maintaining a similar mass concentration to the highly glycosylated case (w.o. $\rho = 226.6$ kg/m³). To approach a system more closely resembling reality, a system containing 30 randomly glycosylated peptides was selected (w. $\rho = 160.5$ kg/m³). Furthermore, to investigate the impact of glycans, a system with 73 nonglycosylated peptides was considered to have the same mass density (w.o. $\rho = 158.6$ kg/m³). The specific fragments considered for each system as well as additional simulation details can be found in Table S9.

The simulation box was filled with peptides adopting different conformations (taken from the single-chain MD simulations), TIP4P-D water molecules, 150 mM NaCl, and extra neutralizing ions. A summary of the simulated systems, the total number of water molecules and ions, as well as the resulting system sizes are presented in Table S9. Each system was equilibrated for 200 ns. Final conformations from this equilibration were considered for subsequent simulations under shear flows. Additionally, two EMD simulations of 2000 ns each were conducted for each multichain system to estimate viscosity at zero shear (see below). The simulation parameters and equilibration protocol were identical to those used in the simulations of single chains (see the section *Single-Chain EMD Simulations* above).

Zero Shear Viscosity. Due to computational constraints, NEMD simulations for very low shear rates were not feasible within the scope of our resources. To address this limitation, we calculated zero shear viscosity using EMD simulations. In this study, the Green–Kubo method (GK)^{59,60} was utilized to estimate zero shear viscosity in the realm of EMD simulations. The GK method allows for the determination of viscosity by integrating the autocorrelation function (ACF) of the pressure tensor components over time. Mathematically, viscosity (η) is determined through the following equation^{41,61}

$$\eta = \frac{V}{k_B T} \int_0^\infty \langle P_{\alpha\beta}(t) \cdot P_{\alpha\beta}(0) \rangle dt \quad (1)$$

where $\langle P_{\alpha\beta}(0)P_{\alpha\beta}(t) \rangle$ is the correlation function of the $\alpha\beta$ component of the pressure tensor (where α and β refer to x , y , and z coordinates and the brackets indicate ensemble average). Here, V , k_B , T , and t denote the simulation box volume, Boltzmann constant, temperature, and time, respectively. Note that here we considered all six independent diagonal and off-diagonal components of the pressure tensor to calculate the ACF and thereby the zero shear viscosity: $P_{\alpha\beta} = P_{xy}, P_{xz}, P_{yz}, (P_{xx} - P_{yy})/2, (P_{xx} - P_{zz})/2,$ and $(P_{yy} - P_{zz})/2$.^{62,63}

For estimating the zero shear viscosity, we focused on three specific systems: 30 nonglycosylated (w.o.), 30 medium glycosylated (w.), and 30 highly glycosylated (w.+) systems. The GK method is acknowledged for its effectiveness primarily in fluids exhibiting relatively low viscosity, typically below 20 mPa s.^{64,65} (Consequently, employing this approach to determine the zero shear viscosity for

nonglycosylated systems with medium and high mass density (w.o. 73 and w.o. 101 chains) is challenging, due to their high expected viscosity.) Our approach consisted of conducting two prolonged simulations (2000 ns) for each system within the NPT ensemble. Subsequently, to ensure a comprehensive sampling of the viscosity of the systems, we extracted 25 conformations every 8 ns from the last 200 ns of each of the two 2000 ns equilibrium simulations (50 extracted conformations in total). Each of these configurations underwent an initial equilibration phase of 2 ns in the NPT ensemble, followed by a subsequent simulation of 20–100 ns in the NVT ensemble to obtain zero shear viscosity. Due to the high fluctuations of the pressure tensor to obtain a reliable estimate of the ACF, in these subsequent simulations, the pressure tensor components were written with a higher output frequency of 10 fs. Accordingly, the zero shear viscosity η was determined by averaging the results of the six distinct pressure components and over the estimates from the 50 distinct high-frequency short trajectories. The average was carried out after the viscosity converged in a time window (Figure 4A–C).

MD Simulations under Shear Flows. To further investigate the influence of shear flow on the viscosity of conglomerates containing lubricin fragments, we conducted shear-driven NEMD simulations using the shear deformation method. The shear viscosity of the system can be determined by applying a Couette flow to the system.⁶⁶ To generate a planar Couette flow, we considered the box deformation method and Lees–Edwards periodic boundary conditions^{67,68} (Figure 2D). In brief, the simulation box was deformed by moving the upper wall of the simulation box (i.e., located at $z = h$, with h the box size dimension along the z axis) laterally at a constant speed u along the x axis (Figure 2D). The x component of the velocity of all particles contained in the simulation box was updated accordingly. This method provides a robust approach to generate planar Couette flow, with shearing occurring in the x direction while the velocity gradient goes along the z direction. In Couette flow, the velocity of the moving wall and the separation between the walls determine the shear rate ($\dot{\gamma}$)

$$\dot{\gamma} = \frac{u}{h} \quad (2)$$

The shear viscosity (η) can be determined by evaluating the ratio between the component of the pressure tensor $\langle P_{xz} \rangle$ and the shear rate of the fluid

$$\eta = \frac{\langle P_{xz} \rangle}{\dot{\gamma}} \quad (3)$$

Here, we use the ensemble average of the components of the pressure tensor. The simulation box was deformed using a GROMACS-2023-dev version,⁶⁹ with the Lees–Edwards boundary condition implemented. In these simulations, the pressure was not maintained constant, and seven distinct deforming speeds were considered: $u = 0.5, 1.0, 2.0, 4.0, 8.0, 10.0,$ and 15.0 nm/ns. The h value was equal to 15.9 ± 0.1 nm in all systems. Accordingly, the resulting shear rates were 0.03, 0.06, 0.13, 0.25, 0.51, 0.63, and 0.95 ns⁻¹, respectively. Simulations of 50–600 ns in length were performed (Table S10), and the pressure tensor component was retrieved from these simulations.

Viscosity of Pure Water. To validate our simulation protocol, we computed the viscosity of the pure water. For the determination of zero shear viscosity, we used a box containing approximately 7100 TIP4P-D water molecules with dimensions of $6 \times 6 \times 6$ nm³. Subsequently, for nonzero shear viscosities, a box with around 4300 TIP4P-D water molecules and dimensions of $8 \times 4 \times 4$ nm³ was selected. The viscosity was computed at a temperature of 310 K, following the same simulation protocol as that for the lubricin fragments, both at zero shear and under shear rates of 0.25, 0.50, 0.99, 1.99, and 2.48 ns⁻¹. Simulation parameters and algorithms were identical to those used in the lubricin simulations, with the exception of the simulation time for nonzero shear rates, where simulations of 20–120 ns in length were performed.

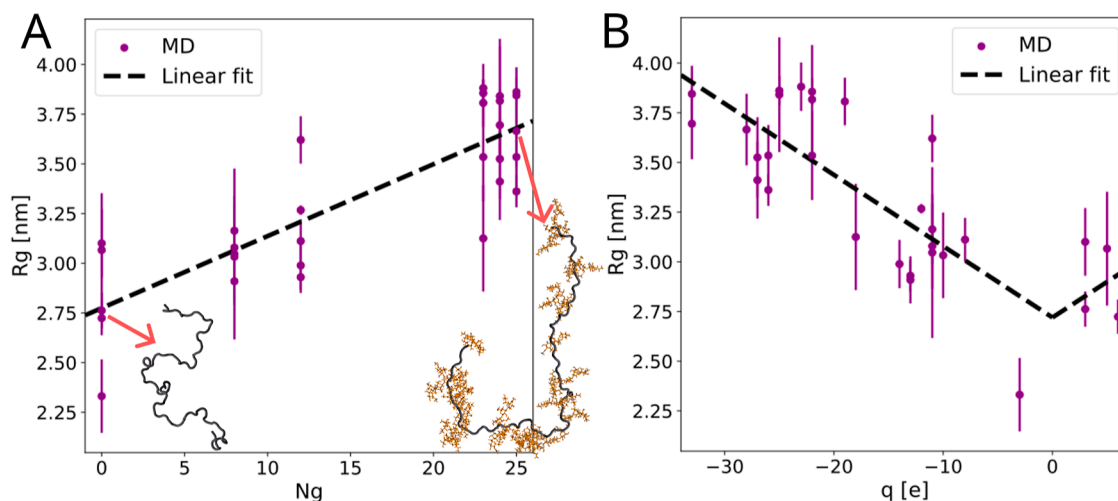


Figure 3. O-glycosylation increases extension and stiffness of lubricin's single-chain fragments. (A,B) Radius of gyration r_g as a function of the number of glycosylated residues N_g (A) and the net charge of the fragment q (B). Symbols display the values recovered from the MD simulations (average \pm s.e., $n = 3$). Dashed lines correspond to a linear regression of the data of the form $r_g = a_N N + b_N$ (A) and $r_g = a_q |q| + b_q$ (B), with resulting fitting parameters $a_N = 0.036$ [nm] and $b_N = 2.77$ [nm] (A) and $a_q = 0.036$ [nm/e] and $b_q = 2.72$ [nm] (B). Cartoons exemplify compact and extended conformations for a fragment without and with bound sugars, respectively (protein: black, sugars: orange).

Simulation Analysis. In addition to viscosity, the following observables were extracted from the molecular simulations. These quantities were computed as ensemble averages after discarding the first half of the simulations as the equilibration time. Statistical uncertainties were reported as σ/\sqrt{n} , where σ corresponded to the standard deviation and n the number of independent samples.

Radius of Gyration. To assess the size of the different fragments, we utilized the radius of gyration. It was extracted from the equilibrium and nonequilibrium simulations by using the GROMACS tool.⁴⁸

Solvent-Accessible Surface Area. To monitor the aggregation between chains, we used the solvent-accessible surface area (SASA)⁷⁰ as a quantitative measure. SASA measures the surface area of a protein or the aggregation of proteins that is exposed to the surrounding solvent molecules. In our analysis, we calculated the value $S = S_T / \sum_{k=1}^{\# \text{chains}} S_k$, where S_T and S_k are equal to SASA of whole chains together and SASA of individual chains, respectively. When S equals 1, it indicates complete dissociation of the chains, implying that they are not interacting with each other. Conversely, a low S value approaching 0 suggests a high degree of association among the chains, implying the formation of a condensed or aggregated state.

Nematic Order. The nematic correlation function (NCF) was computed to analyze the propensity of the chains to align with respect to each other. It delves into the orientation of individual polymer chains, concerning each other. The NCF, typically denoted as $\Pi_{ij}(r)$, is calculated by considering pairs of amino acids, i and j , from two different protein backbone chains I and J , at a specific distance from each other within the system⁷¹

$$\Pi_{ij}(r) = \langle |\mathbf{t}_i \cdot \mathbf{t}_j| \rangle = \frac{\sum_I \sum_{J>I} \sum_{i \in I} \sum_{j \in J} |\mathbf{t}_i \cdot \mathbf{t}_j| \delta(|\mathbf{r}_i - \mathbf{r}_j| - r)}{\sum_I \sum_{J>I} \sum_{i \in I} \sum_{j \in J} \delta(|\mathbf{r}_i - \mathbf{r}_j| - r)} \quad (4)$$

The value of $\Pi_{ij}(r)$ falls within the range of 0.5 to 1.0. A value of 0.5 indicates a complete absence of alignment, signifying that the orientation of fragments is entirely stochastic. Conversely, a value of 1.0 signifies perfect alignment, where the fragments exhibit uniform orientation.

GROMACS analysis tools were utilized to extract the simulation observables. Further postprocessing of the data was carried out by using in-house Python scripts. Trajectories were visualized and snapshots were rendered with VMD.⁷²

Continuum Simulations. To highlight the transferability of our molecular characterization of viscosity and shear thinning in a

multiscale approach, we performed exemplary continuum simulations with fluid models that are informed by our MD data. Therefore, we solve the one-dimensional steady Reynolds equation for an incompressible fluid

$$\frac{d}{dx} \left(\frac{h(x)^3}{12\eta} \frac{dp}{dx} - \frac{Uh(x)[1 - \theta(x)]}{2} \right) = 0 \quad (5)$$

which is a simplification of the Navier–Stokes equation for laminar thin-film flows including mass-conserving cavitation handled via the Jakobsson, Floberg, and Olsson^{73,74} formalism. Equation 5 can be solved for the pressure distribution $p(x)$ in a thin gap, given its height profile $h(x)$ and a constant entrainment speed U . The cavity fraction $\theta(x) = 1 - \rho(x)/\rho_0$ discriminates between full film ($\theta = 0$) and cavitated regions ($0 < \theta \leq 1$), where ρ_0 is the full film density. The Reynolds equation is accompanied by a complementarity constraint $(p - p_{\text{cav}})\theta = 0$ to ensure that the pressure does not fall below a certain threshold p_{cav} (the vapor pressure) in the cavitated regions. We solve the so obtained linear complementarity problem with the Fischer–Burmeister–Newton–Schur algorithm,⁷⁵ where the first and second term in eq 5 are discretized with a central difference and a first-order upwind scheme, respectively.

The Reynolds equation was originally derived for isoviscous fluids,⁴³ but high pressures and shear rates in confined fluids often require the consideration of non-Newtonian effects such as piezoviscosity or shear thinning. Including these nonlinearities into the Reynolds equation is not always straightforward,⁷⁶ but substituting the constant viscosity in eq 5 with an appropriate model $\eta(\dot{\gamma}, p)$ leads to good approximations in most cases. The solution to the nonlinear problem is then found via fixed-point iteration. A common way to describe shear thinning is the Carreau–Yasuda equation

$$\eta(\dot{\gamma}) = \eta_0 (1 + (\lambda \dot{\gamma})^a)^{(n-1)/a} \quad (6)$$

which describes the shear rate dependence of the viscosity as a power law with exponent $n < 1$ for $\dot{\gamma} \gg \lambda^{-1}$ and approaches a Newtonian plateau at low shear rates. The Yasuda parameter a controls the transition between power law and Newtonian behavior and takes the values $a = 2$ and $a = 1 - n$ for two prominent shear thinning models, namely the Carreau model⁴⁴ and the Cross model,⁷⁷ respectively. We found that the Carreau model consistently described our data better than the Cross model (see Figure S3). We assume homogeneous shear thinning across the gap, i.e., the velocity profiles do not deviate

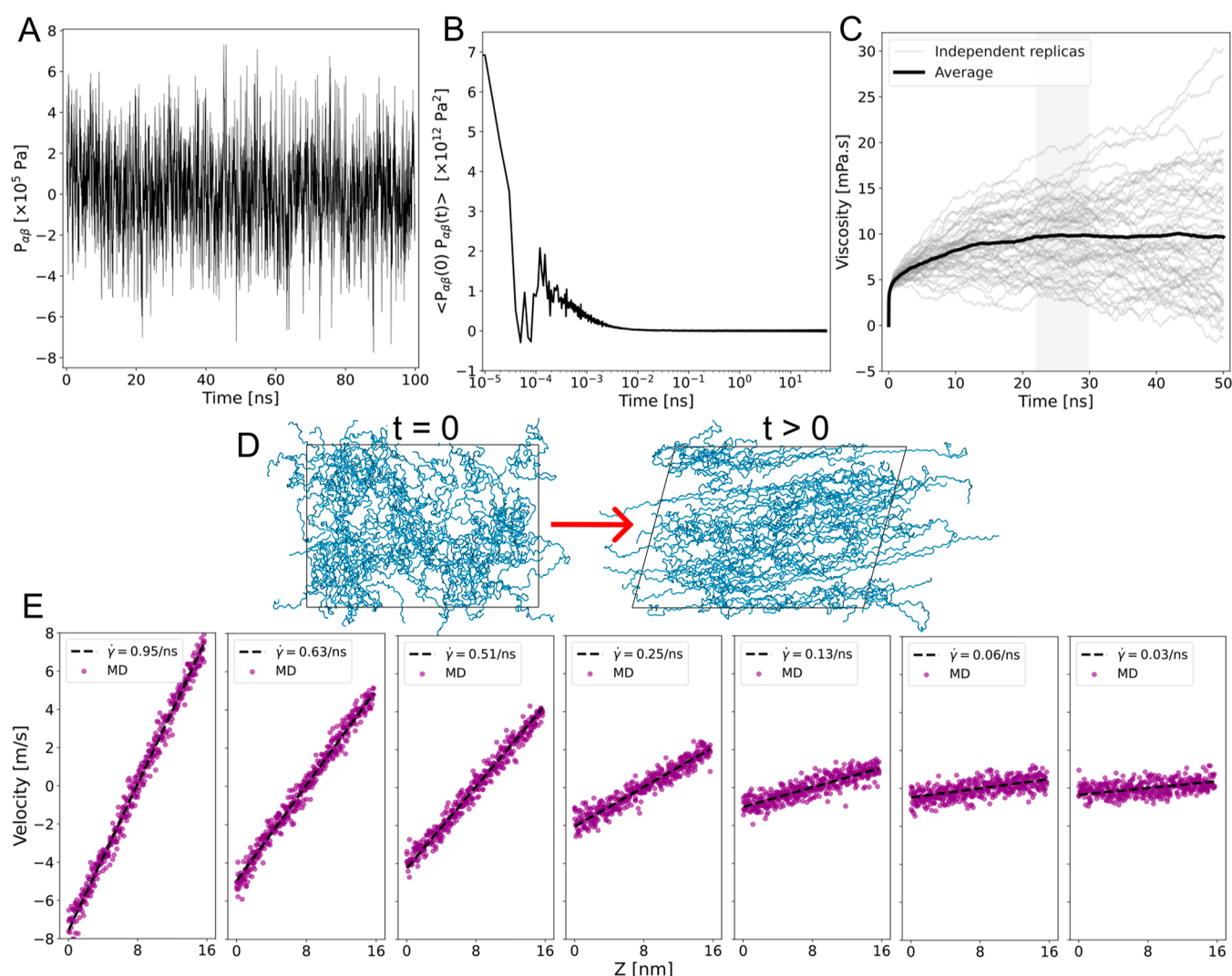


Figure 4. Viscosity calculation procedure at zero shear (A–C) and under shear flows (D,E). (A) Components ($P_{\alpha\beta}$) of the pressure tensor extracted from EMD simulations (shown here is the time-trace of one component for an exemplary system). (B) The average of autocorrelation of all pressure components is computed for each independent system. (C) The zero shear viscosity is obtained from the average autocorrelation of all pressure components using eq 3 (see Materials and Methods). Gray curves represent the independent viscosity of each replica ($n = 50$). The black curve displays the average of all these curves. The viscosity was extracted from the plateau-highlighted region (average \pm standard error). Figure S7 shows all three cases of zero shear viscosity. (D) To estimate the shear viscosity, the simulation box was deformed at a shear rate $\dot{\gamma}$. Initial ($t = 0$) and posterior ($t > 0$) snapshots are shown, highlighting the lubricin fragments in blue. (E) Velocity profiles were obtained upon box deformation under different shear rates. The line corresponds to the linear fit. Output shear rates, i.e., u/h , are shown in the legend. Also, the expected values of shear rates are 0.94, 0.625, 0.50, 0.25, 0.125, 0.06, and 0.03 ns^{-1} .

from the Newtonian ones but the effective viscosity is reduced according to eq 6 with an average shear rate $\dot{\gamma}_{\text{avg}} = (|\dot{\gamma}_{\text{bot}}| + |\dot{\gamma}_{\text{top}}|)/2$, where $\dot{\gamma}_{\text{bot}}$ and $\dot{\gamma}_{\text{top}}$ are the shear rates at the bottom wall and top wall, respectively. Note that this is a reasonable assumption only for weakly shear thinning fluids or for fluids where Couette flow dominates. For a more rigorous treatment of shear thinning, application of the generalized Reynolds equation⁷⁸ might be necessary.

RESULTS

Glycosylation Expands the Conformation of Lubricin Fragments. Lubricin is a very large glycosylated protein with a central disordered region of approximately 800 amino acids (Figure 1B). Simulating such a long, disordered protein is prohibitively expensive at the atomistic level of resolution. To elucidate the impact of O-glycans on the conformation of lubricin, we selected five 80-amino acid segments within the central disordered region (as depicted in Figure 1B). These

segments vary in their number of glycosylation sites, as well as contents of proline and charged residues. Subsequently, we generated five distinct glycan distributions for each of these segments by randomly attaching the six types of O-glycans according to their average proportions found in lubricin to all known O-glycosylation sites of the segment (Figure 1C, also see Materials and Methods).^{13,15} We repeated this procedure five times for each segment, which resulted, together with a nonglycosylated almost neutral state, in six different charge patterns per segment (Figure 1D,E). In a first step toward bulk lubricin solution systems for simulations under shear, we generated equilibrium structural ensembles considering single fragments, i.e., under infinitely diluted conditions. We conducted multiple 200 ns MD simulation replicas for this purpose (Figure 2A,B). These fragments later served as starting points for assessing the viscosity of systems of solutions with high lubricin concentrations (Figure 2C,D, next section).

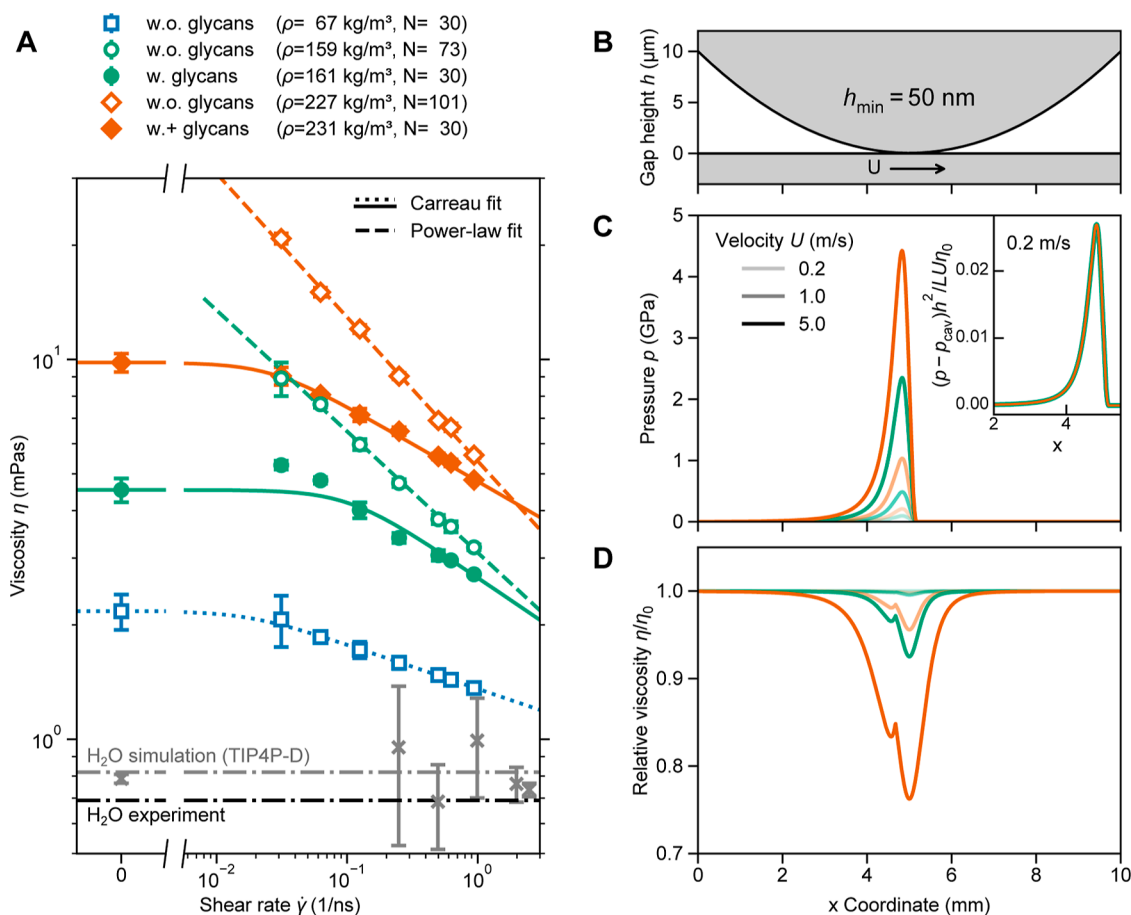


Figure 5. Shear thinning behavior of glycosylated lubricin fragments. (A) Viscosity η as a function of the shear rate $\dot{\gamma}$ obtained from equilibrium simulations ($\dot{\gamma} = 0$) and shear-driven NEMD simulations ($\dot{\gamma} \neq 0$). Five different systems were considered, either without glycans (“w.o.”: open symbols and dashed or dotted lines) or with glycans (“w.”: closed symbols and solid lines). Systems with medium (“w.”: green) and high (“w.+”: orange) levels of glycosylation were considered at the indicated mass (ρ) and molar densities (with N indicating the number of peptides in the system). A low-density system without glycans was also simulated (blue). For systems where zero shear Newtonian viscosities are available, fits to the Carreau model (eq 6, $a = 2$) are shown (solid or dotted lines). Dashed lines are fitted to a simple power law expression $\eta \propto \dot{\gamma}^{n-1}$ without a Newtonian plateau. The viscosity of water, both experimental and obtained here, is also displayed as reference (gray and black, respectively). (B) Sample geometry for Reynolds calculations with a flat wall sliding at velocity U against a parabolic height profile $h(x) = h_{\min} + 4(h_{\max} - h_{\min})(x/L_x - 1/2)^2$ with $h_{\min} = 50$ nm, $h_{\max} = 10$ μm , and $L_x = 10$ mm. (C) Pressure profiles for lubricants with medium and high levels of glycosylation and three different sliding velocities. At low speed, normalized pressure profiles (by a reference pressure $\eta_0 L U / h^2$) fall onto the same curve, indicating that the flow is still in the Newtonian regime, as shown in the inset. (D) Effect of shear thinning in the Reynolds calculations shown by the local relative viscosity $\eta(\dot{\gamma})/\eta_0$ along the sliding direction.

To quantify the size of the fragments, we computed the radius of gyration (R_g). The glycans are bulky side chains that are expected to contribute to the overall radius of gyration of the fragments. However, to be able to assess the effect of glycosylation on the size of the fragments, we only considered the backbone atoms for the radius of gyration calculation. Starting from fully stretched conformations, within a few tens of nanoseconds, the fragments partially collapsed, adopting conformations that ranged from approximately 2.3 to 3.9 nm (Figure S4). Figure 3A illustrates the correlation between equilibrium R_g and the number of glycosylated residues per fragment. As expected, the more glycosylation sites are introduced, the more extended the conformation adopted by the fragments. The O-linked glycans attached to lubricin vary in composition, and several of them carry a negative net charge (Figure 1C). This imposes an abundance of negative charge along the lubricin sequence (Figure 1D,E). Consequently, the size of the fragments increased by augmenting their net charge (Figure 3B), as previously observed for other intrinsically

disordered proteins (IDPs).^{45,46} Note that the end-to-end distance or the SASA, which are other quantities indicative of the extension of the chains, consistently showed a trend similar to that of the radius of gyration (Figures S5 and S6). A linear fit of the data of the form $r_g = a_q |q| + b_q$ yielded a slope of $a_q = 0.036$ nm/e, which is about one-fourth smaller than the value obtained in previous studies on IDP phosphorylation^{45,46} (i.e., 0.048 nm/e). The higher ionic strength of 150 mM used here (as opposed to 100 mM in refs 45 and 46), by screening the electrostatic interactions further, may be responsible for the weaker response of r_g to changes in charge observed here. In addition, the fit retrieved an intercept $b_q = 2.72$ nm, which is very close to the estimate for a random coil adapted to IDPs⁷⁹ ($R_c = R_0 N^{0.588} = 2.61$ nm, where $R_0 = 0.19$ nm and N is the number of amino acids, specifically $N = 80$ in our case). In previous studies, the intercept was significantly smaller [1.7(1) nm^{45,46}]. The intercept is indicative of overall size of the chains under neutral conditions. In such case the bulky sugars, presumably acting as spacers, tend to promote more expanded

conformations of the lubricin backbone fragments as compared as other IDP fragments with comparably smaller standard⁴⁵ or phosphorylated⁴⁶ amino acid side chains. Thus, O-glycans possess the capability to strongly expand the conformation of single-chain lubricin fragments. In the following, we investigated how lubricin influenced its medium's viscosity.

Viscosity. We next asked how O-glycans impact the rheological properties of lubricin. We calculated the viscosity of mixtures of fragments taken from the disordered region of lubricin in solution by conducting equilibrium and shear-driven NEMD simulations (Figure 2C,D). Systems with different protein content (both in mass and molar density) as well as different levels of glycosylation were considered (see Materials and Methods and Table S9). Additionally, we computed the viscosity of pure water to validate our protocols. First, we employed the GK method to calculate the zero shear viscosity from the autocorrelation of the pressure tensor (see Figure 4A–C and Materials and Methods section, Zero Shear Viscosity) calculated from EMD simulations. Note that this method is primarily applicable to fluids exhibiting low viscosity, typically below 20 mPa s.^{64,65} Consequently, it was not employed for the medium and high nonglycosylated systems as the simulations with shear for these systems indicated a trend toward significantly larger zero shear viscosities (see below). Second, the box deformation method and the Lees–Edwards periodic boundary conditions were used to obtain a Couette flow (Figure 4D,E and the Materials and Methods section MD Simulations under Shear Flows). The resulting velocity profiles linearly changed with the input shear rate (Figure 4E). Thus, this method enabled the utilization of eq 3 to estimate the viscosity of the system under different shear rates based on the pressure along the shearing direction.

Figure 5A displays the resulting viscosities under different shear rates and at zero shear viscosity. As expected for a Newtonian fluid, the viscosity of pure water did not change in the presence of shear. Furthermore, the obtained values were close to the experimental and the computational value⁸⁰ of 0.693 mPa s (at the temperature of 310 K used throughout the simulations). Consequently, these results for water validate our simulation protocol and serve as a reference to examine the viscosity of systems with lubricin fragments.

The systems containing lubricin fragments featured viscosities higher than those of the system composed of only water. Unlike pure water, the viscosity of these systems changes with each shear rate, and with the increasing shear rate, the calculated viscosity decreases slightly, indicating that these systems transition to a non-Newtonian regime exhibiting shear thinning behavior (Figure 5A). The change in viscosity with shear varied drastically among the different systems. Reduction in the protein mass density decreased the viscosity, approaching the value observed for pure water (compare curves for different densities, i.e., different colors). A further reduction in sensitivity to shear (i.e., the slope in the viscosity–shear curve) was observed for the glycosylated systems compared to their nonglycosylated counterparts (compare non- and glycosylated systems, i.e., dashed with solid lines). Within the same mass density, the glycosylated systems (solid lines) exhibited lower viscosity compared to nonglycosylated (dashed lines) counterparts.

A Carreau model (eq 6 with fixed $a = 2$) explains well the viscosity–shear relationship obtained for the systems for which zero viscosity was computed (Figure 5A and Table 1).

Table 1. Fitting Analytical Models to the Viscosity–Shear Curves Obtained from MD Simulations^a

system	ρ (kg/m ³)	N	η_0 (mPa s)	n (-)	λ (ns)
w.o. glycans	66.5	30	2.173	0.884	56.7
w.o. glycans	158.6	73		0.681	
w. glycans	160.5	30	4.535	0.766	9.7
w.o. glycans	226.6	101		0.622	
w.+ glycans	230.6	30	9.813	0.802	38.1

^aFive different systems were considered, either without glycans (“w.o.”) or with glycans (“w.”), at the indicated mass (ρ) and molar densities (with N indicating the number of peptides in the system). For systems where zero shear Newtonian viscosities were available, the Carreau model (eq 6, $a = 2$) was applied, yielding three fit parameters: zero shear viscosity η_0 , the exponent n , and the scaling factor λ . For systems lacking zero shear viscosities (-), a simple power law expression $\eta \propto \dot{\gamma}^{n-1}$ retrieved the parameter n .

However, such an analytical model could not be applied to the systems lacking zero shear viscosity, namely the medium- and high-density nonglycosylated ones (Figure 5A). A simple power law expression, without the Newtonian plateau, was fitted in these cases instead, and it also explained the simulation data well (Figure 5A and Table 1). The Carreau fit retrieved zero shear viscosities that were largely dependent on protein density. Note that although the medium- and high-density nonglycosylated systems lacked a direct estimate of the zero shear viscosity, extrapolation of their viscosity toward low shear rates suggests the zero shear viscosity to take even larger values for these two systems than the glycosylated ones (Figure 5A). The shear rate at which the system transitioned from a Newtonian to a non-Newtonian regime is related to $1/\lambda$ (see eq 6). This value was on the order of 10^{-2} to 10^{-1} ns⁻¹. Both models predicted an exponent n which measures the extent of decrease in viscosity with the shear rate, where small values of n indicate strong shear thinning. These values are comparable across systems, although they are consistently higher for the glycosylated systems (compare n for systems with and without glycans in Table 1).

In summary, our data demonstrate, in the high shear regime, a pronounced shear thinning behavior of lubricin mixtures and its strong modulation exerted by the presence of O-glycans.

Effects of Shear Thinning in Macroscopic Simulations. To show possible applications of the shear thinning models to macroscopic systems, we performed continuum simulations that highlight the effect of lubricin's viscosity on pressure profiles generated in a lubricated sliding contact. We focused on a simplified setup that consists of a parabolic gap height profile sliding at speed U against a flat wall (although we have chosen the frame of reference to be located on the profiled surface for simplicity, see Figure 5B). Furthermore, we assumed that the profile extends infinitely into the direction perpendicular to the sliding velocity and gap height.

The solution to Reynolds eq 5 provides pressure profiles that are generated in front of the geometrical constriction, as shown in (Figure 5C). For a given geometry, the pressure excursions depend on viscosity and sliding speed only. Here, we compare the medium (green) and highly (orange) glycosylated configurations for three different sliding speeds $U \in [0.2, 1.0, 5.0]$ m/s as indicated by the level of line opacity. It is not surprising that increasing either the sliding velocity or viscosity (by increasing the level of glycosylation) leads to higher pressures. Behind the constriction, the fluid film cavitates, and

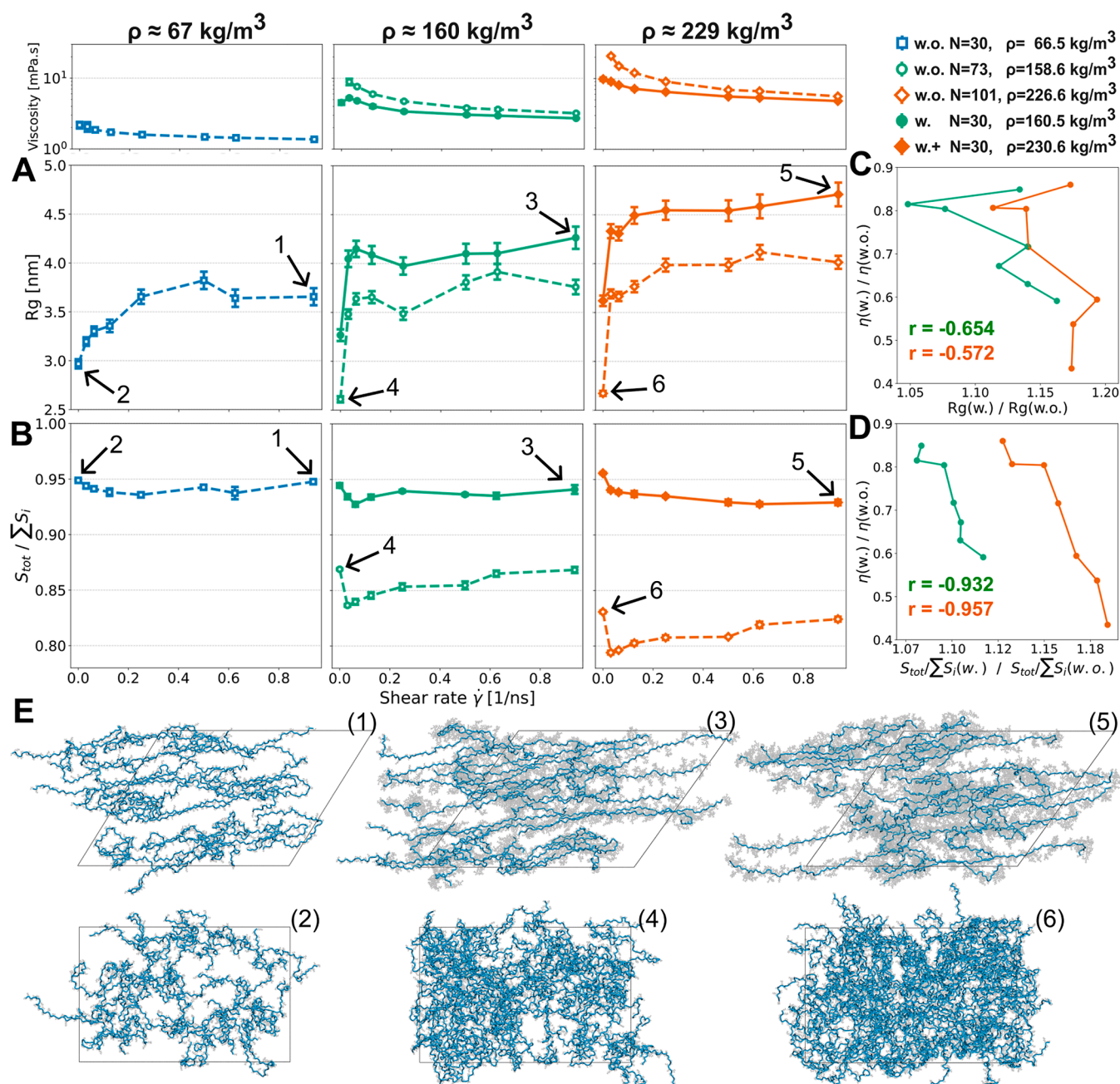


Figure 6. Shear-dependent rheological properties of lubricin fragments derived from MD simulations. (A,B) Variation of the radius of gyration (R_g) and the ratio between the SASA of whole proteins and the cumulative SASA of individual proteins (surface exposure ratio, see [Materials and Methods](#) section) (B) as a function of the shear rate ($\dot{\gamma}$). Low values of $S_{\text{tot}}/\sum S_i$ indicate a high degree of protein aggregation, whereas a value of one denotes zero aggregation. Symbols represent data obtained from EMD simulations at zero shear rate and shear-driven NEMD simulations at nonzero shear rates (average \pm standard error, $n = 4$). Dashed lines correspond to nonglycosylated systems (“w.o.”), while solid lines represent glycosylated ones (medium glycosylated: “w.” and highly glycosylated: “w.+”). Color indicates mass densities. The viscosity–shear response (see [Figure 5A](#)) is shown at the top of A for comparison. (C,D) The ratio of viscosity $\eta(w.)/\eta(w.o.)$ is presented as a function of the ratio $X(w.)/X(w.o.)$, with $X = R_g$ (C) and $X = S_{\text{tot}}/\sum S_i$ (D), in both the medium (green) and high (orange) mass density regimes. Correlation coefficients (r) for each data set are indicated. (E) Representative snapshots for the extreme cases highlighted with arrows in A and B are shown (backbone: blue and (un)glycosylated side chains: gray).

the pressure equals the cavitation pressure. The load-bearing capacity, i.e., the force per unit length theoretically required to maintain the predefined gap height distribution (without considering elastic deformation of the walls) reaches 2.6 kN/mm for the highest pressure excursion (highly glycosylated and $U = 5 \text{ m/s}$).

Looking at the pressure profiles alone does not elucidate the effect of shear thinning. In the Newtonian, i.e., linear response

regime, normalized pressure profiles fall onto the same curve, which was only approximately true for the lowest sliding velocity as shown in the inset of [Figure 5B](#). In contrast, the highest sliding velocity led to non-Newtonian flows as illustrated in the viscosity profiles along the contact line in [Figure 5D](#). We observed viscosity reduction down to less than 95 and 80% of the Newtonian viscosity at the point where the magnitude of the pressure gradient is largest for the medium

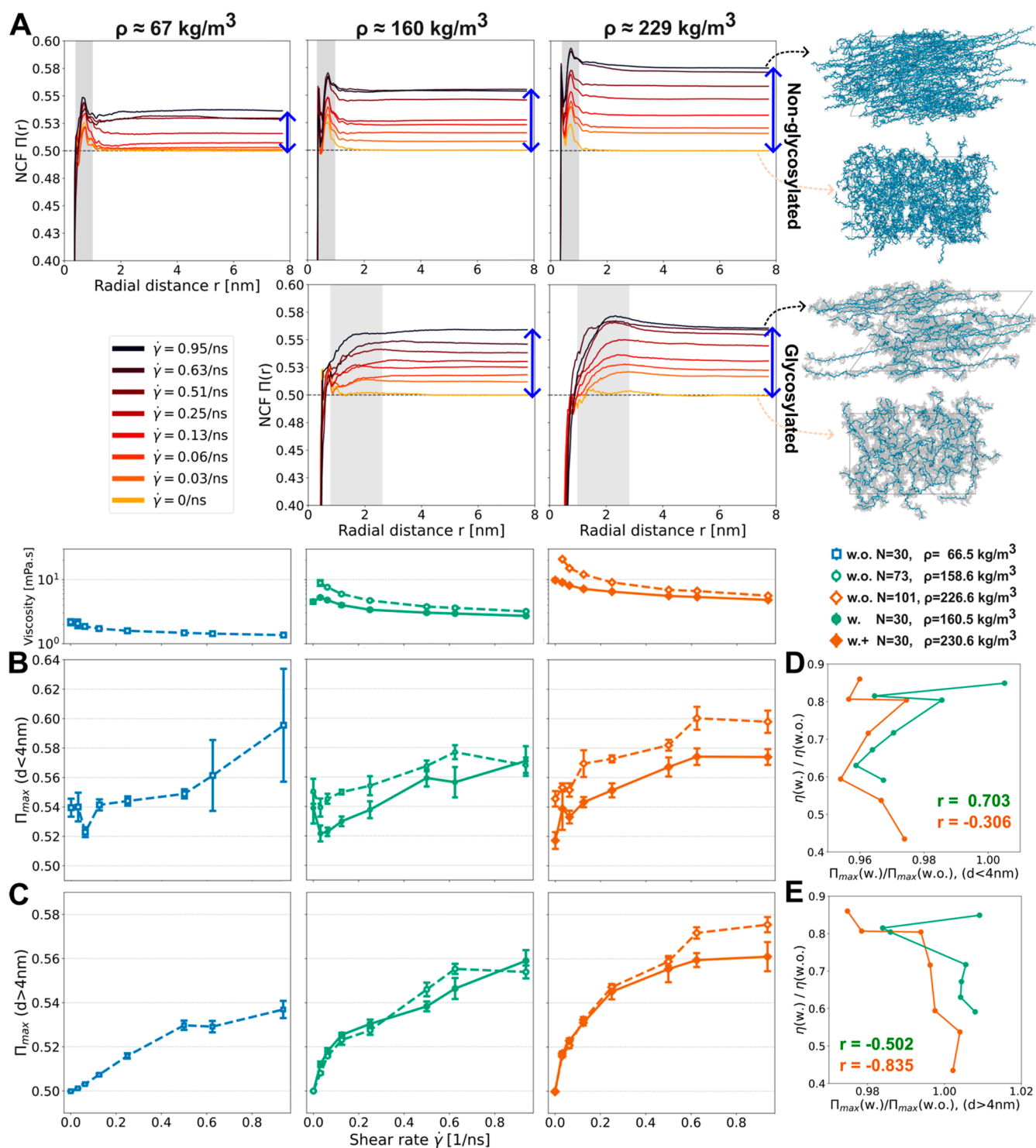


Figure 7. Shear-dependent alignment of lubricin fragments derived from MD simulations. (A) NCF for bulk systems of nonglycosylated (top row) and glycosylated (bottom row) systems with different mass concentrations (columns) as a function of the radial distance. Color indicates the different shear rates. An NCF value of 0.5 indicates random chain orientation, while 1.0 indicates full alignment. The gray area corresponds to nearest neighbors region for which high alignment was observed. Representative snapshots for the extreme cases, highest and lowest shear rates, are shown (backbone: blue and (un)glycosylated side chains: gray). (B,C) NCF for short-range (<4 nm) (B) and for long-range (>4 nm) (C) interchain separations as a function of the shear rate ($\dot{\gamma}$). Symbols depict data obtained from the simulations (average \pm standard error, $n = 4$). Dashed lines correspond to nonglycosylated systems (“w.o.”), while solid lines represent glycosylated “w.” systems. Colors indicate mass density. The viscosity–shear response (of Figure 5A) is shown at the top of B for comparison. (D,E) The ratio $\eta(w.)/\eta(w.o.)$ is presented as a function of the ratio $X(w.)/X(w.o.)$, with $X = \text{NCF}_{\text{max}}$ i.e., the maximum of the NCF, at short-range (C) and long-range (D) separations, in both the medium (green) and high (orange) mass density regimes. Correlation coefficients (r) for each data set are indicated.

and highly glycosylated systems, respectively. Direct comparison of shear thinning for glycosylated and nonglycosylated

peptides with our Reynolds calculations is difficult because our MD data does not resolve the Newtonian plateau for the latter.

However, we expect a much higher shear thinning for systems without glycans, as reflected by the exponents from the fits to the Carreau and the power-law models, see Table 1. In the shear thinning regime, a 10-fold increase of the shear rate reduces the viscosity by 37% in the system with high level of glycosylation ($n = 0.80$), compared to 58% in the system without glycans ($n = 0.62$).

Rheology of Lubricin under Shear Stress. We next investigated the molecular causes that gave rise to the observed shear thinning behavior of the systems containing mixtures of lubricin fragments. We analyzed distinct structural attributes within these mixtures related to the elongation, aggregation, and alignment responses of the lubricin fragments under the influence of external shear stress.

We first analyzed the elongation of individual chains within the mixture by computing their radius of gyration (R_g). Figure 6A displays the impact of shear stress on the R_g . In all cases, an increase in the shear rate induced an increase in R_g , indicating that the chains adopt more elongated conformations under shear stress. The reference value at zero shear displayed a strong dependency on mass density and glycosylation: as the mass density increased, glycosylated unsheared chains were found to be more elongated, while the nonglycosylated unsheared ones were more compact (compare zero shear values for different mass densities and glycosylation in Figure 6A). The elongation response under shear was also dependent on these two factors. Sheared glycosylated chains were found to be more elongated as the mass density increased, an effect that could be attributed to the electrostatic repulsion between the negatively charged sugars. Surprisingly, nonglycosylated chains also displayed a similar trend, despite lacking such repulsion (see the increasing offset with density in the elongation curves in Figure 6A). However, overall, the elongation of glycosylated chains significantly surpassed that of nonglycosylated counterparts for each mass density.

We next investigated the aggregation tendency of the chains by computing the SASA of the whole protein conglomerate divided by the sum of the SASA values of each individual chain. Accordingly, this ratio takes a maximum value of one when the chains are completely separated, while it diminishes when the chains aggregate (see Materials and Methods section Solvent-Accessible Surface Area). Figure 6B shows the impact of shear flow on the interaction behavior of the lubricin mixtures. In all instances, imposing shear stress results in increased intermolecular interactions between fragments relative to their state under zero shear rates (compare zero vs nonzero values in Figure 6B). Nevertheless, glycosylated and nonglycosylated mixtures displayed a distinct response to shear. Interchain interactions of glycosylated mixtures were overall low and practically insensitive to shear and to mass density (see high SASA ratio and practically constant values for different shear and density conditions). On the contrary, nonglycosylated chains displayed a strong level of interactions (low SASA ratio) directly proportional to mass density but inversely related to shear (see a monotonic increase in the SASA ratio with shear with an augmenting offset as density increased for the nonglycosylated chains).

The third structural attribute that we investigated was the alignment of the lubricin chains, assessed by computing the NCF. This function monitors the correlated orientation of all chains weighted by their radial distribution function (see Materials and Methods section Nematic Order). Figure 7A illustrates that across all scenarios higher shear rates lead to a

stronger alignment of chains. Higher shear rates enhance chain alignment for both nearest neighbor chains (Figure 7B) and distant chains (Figure 7C), as also visible from exemplary snapshots shown in Figure 7A. Note that due to the bulky glycan side chains, the distance to the first aligned neighbor was found to be higher for the glycosylated systems, indicating more spacing between these chains (Figure 7A). This is another indication of the low level of interaction in this case (Figure 6B). Within nonglycosylated systems, increasing the mass density results in a greater degree of alignment (Figure 7A), both locally for the first-neighbor chains (Figure 7B) and for distant chains (Figure 7C). Conversely, in glycosylated systems, alignment is less sensitive to changes in the density (Figure 7A). Glycosylated chains align in a less correlated fashion with their nearest neighbors and pretty much equally with the distant ones, compared to the nonglycosylated ones (compare glycosylated vs nonglycosylated cases in Figure 7B,C).

To connect these structural characteristics with viscosity, we computed the ratio of viscosity between glycosylated and nonglycosylated systems and compared it with the corresponding ratio of the radius of gyration, SASA ratio (Figure 6C,D), and nematic order parameter (Figure 7D,E). This analysis suggests that the divergent shear thinning trend observed between glycosylated and nonglycosylated systems is more closely correlated with interchain interactions, that is, clustering of chains, than with their relative ordering (see higher correlation in Figure 6D than in Figures 6C and 7D,E).

In summary, the structural response of conglomerates to shear is tightly controlled by both the protein density and the extent of glycosylation.

DISCUSSION

By using atomistic MD simulations under shear, here we investigated the role of O-glycans on the structural and rheological properties of lubricin fragments. A central finding of our study is that the viscosity and shear thinning behavior of mixtures containing short fragments derived from lubricin are tuned by the level of the O-glycosylation of these fragments.

The conformational dynamics of IDPs is tightly regulated by post-translational modifications, such as phosphorylation,^{45,46,81} methylation,⁸² and glycosylation.^{38,83} Lubricin contains a large disordered region that is highly glycosylated (Figure 1B). We here show that glycosylation strongly influences the structural properties of single 80 AA fragments distributed across this disordered region. A notorious difference of glycosylation with other post-translational modifications is the size of the attached moiety. While in phosphorylation or methylation, small moieties are added to side chains, in glycosylation, large and bulky glycans are attached to the protein. This is the case for lubricin which displays a complex and dense glycosylation pattern^{38,83} (Figure 1C). Accordingly, glycosylation promoted more expanded conformations for lubricin fragments than those observed for other IDPs of comparable sequence length^{45,46} (Figure 3). Nevertheless, the size of the fragments linearly increases with their net charge following a similar V-pattern.^{45,46} This emphasizes the important role electrostatics has in governing the conformation of IDPs and the ability of post-translational modifications to tune such conformations. In the case of lubricin, the sensitivity of the conformational ensemble to glycosylation appears to be a crucial determinant of its viscosity response to shear (as discussed below).

To assess the viscosity response to shear, we employed equilibrium and shear-driven NEMD simulations (Figures 2 and 4). As an alternative and more-affordable computational approach to examine the effect of lubricin and, more specifically, its glycosylation on the medium viscosity, we avoided the consideration of the full ~ 800 amino acid long disordered region but instead a mixture of short glycosylated fragments extracted from it. This constitutes the first attempt to resemble the lubricin content in a small volumetric unit. To validate our protocol, we calculated the viscosity of pure water. Importantly, we observed its Newtonian behavior, namely, we obtained a viscosity that is independent of the applied shear (Figure 5A). Moreover, we obtained values which are consistent with the experimental viscosity of water⁸⁴ and with the viscosity estimate for the TIP4P-D water model,⁵⁴ the water model suited for IDPs which has been used in this study. To obtain the viscosity under shear, we performed shear-driven NEMD simulations in which the box was deformed according to the Lees–Edwards periodic boundary conditions, as previously suggested.⁶⁸ We made use of a developmental implementation of such methodology in the GROMACS package⁴⁸ (GROMACS-2023-dev version⁶⁹). We confirmed that in fact this methodology can retrieve sustained planar Couette flows (Figure 4D,E) and can be used to reliably estimate the viscosity of the medium. Consequently, this approach becomes attractive for studying the shear response of other biomolecular systems with the widely used GROMACS package. Note, however, that large deformation velocities had to be applied. We opted for the Lees–Edwards boundary conditions as opposed to two walls moving relative to each other to induce the shear^{67,68} as the latter setup requires appropriate description of the wall–solvent and wall–solute interactions. Such walls are absent in the biological or experimental setting and can induce artifacts. To close the gap between experimental observations, typically at low or zero shear,⁸⁵ and our shear-driven NEMD simulation results, we also computed the viscosity at zero shear, from the autocorrelation of the pressure tensor components, by using the GK method^{41,86} (Figure 4A–C). However, this choice excluded systems exhibiting large viscosities, i.e., $> 20\text{--}30$ mPa s.^{64,65} Medium and highly dense nonglycosylated lubricin systems precisely fell into this category, but they still served as a reference of the overall shear response when glycans were not present. In addition to the viscosity, future research could use the autocorrelation of the pressure tensor to analyze the frequency-dependency of the shear modulus⁸⁷ and thereby provide additional insights of the viscoelastic response of systems containing this glycosylated protein. Furthermore, with the help of the Carreau model (eq 6) we could predict the viscosity for the whole range of shear, and in its absence too, for the glycosylated systems.

Parameterization of semiempirical viscosity models such as the Carreau model can be leveraged in multiscale simulations of lubrication. By doing so, molecular mechanisms to accommodate externally applied shear can be effectively transferred to length and time scales initially inaccessible to MD simulations. The simulation setup in Figure 5B has been chosen without having a specific application in mind and should be primarily seen as a proof of concept. However, it is easy to imagine that the gap height profile could be replaced by the actual topography of an AFM tip or macroscopic synovial joint replicates. Recent macroscopic simulations of synovial joint lubrication, such as those considering pressure-induced

rehydration by cartilage surfaces,⁸⁸ might benefit from MD-informed constitutive relations. Similarly, other effects such as pressure-dependent viscosity, compressibility, or localized shear might be subsequently introduced into hydrodynamic descriptions.⁸⁹

Lubricin acts as a lubricant in the synovial fluid.^{2–6} Ludwig et al. reported viscosities in the range of a few mPa s for full-length recombinant lubricin.⁸⁵ The experimental viscosity continuously increased, in a logarithmic fashion, i.e., it required an increase in density of one decade (from 0.0045 to 0.0450 kg/m³) to display a change of ~ 0.5 mPa s and yet another decade (from 0.045 to 0.450 kg/m³) to display an additional change of ~ 0.5 mPa s (see Figure 2 in Ludwig et al.⁸⁵). Consistent with this behavior, at the 500-fold higher protein density used in our simulations (from 60 to 230 kg/m³), the predicted zero shear viscosities were not far from the experimental ones (Figure 5A). This is an encouraging result. However, the direct comparison between the simulation of experimental viscosities should be done with caution as in simulations, in addition to the much higher density, we had to consider shorter protein chains and exclude the terminal globular domains.

Our simulations together with the Carreau model predict shear thinning to occur at high shear rates ($> 10^{-2}$ /ns i.e. $> 10^7$ /s) and a Newtonian behavior otherwise, for both studied glycosylated systems and the nonglycosylated system at low density (Figure 5 and Table 1). In agreement, at experimentally accessible rate regimes (~ 10 to 10^3 /s), pure glycosylated lubricin exhibits a Newtonian behavior.⁸⁵ Shear rates are believed to vary widely in the synovial joint, reaching $> 10^6$ /s,⁹⁰ and may even exceed this range on the microscopic scale, e.g., due to surface roughness. The role of shear thinning at these larger shear rates, as observed in our simulations, is currently unknown. Larger simulation systems at coarser resolution will be required to more directly address rheology in the physiological setting. Importantly, such systems will allow to consider full-length glycosylated lubricin chains, including the terminal globular ends and thereby to incorporate other physiologically relevant boundary effects such as surface attachment.²⁶ In addition, such approach will permit to consider other synovial components known to also impact fluid viscosity (such as hyaluronic acids).⁸⁵

It is remarkable that despite its simplicity, our model seems to contain the necessary molecular features that give rise to the observed lubricin medium's viscosity. We suspect the key feature is the inclusion of glycosylated stretches from the disordered region (Figure 1). In fact, O-linked glycosylation was found to critically modulate the shear thinning response and the value to which the viscosity approached zero shear (Figure 5A). At a given mass density, glycosylation reduced the medium viscosity (due to steric hindrance and electrostatic repulsion, as explained below). This observation supports the previously reported notion that deglycosylation causes a loss in lubricity of mucins^{19–21} rather than the opposite effect.²² It also can aid our understanding of how changes in glycosylation can compromise the synovial fluid's function in arthritis.^{91,92}

The glycosylation status exerts a significant influence on structural parameters that dictate the fragment's elongation (Figure 6A), interactions (Figure 6B), and alignment (Figure 7). Remarkably, the presence of glycans prevents the formation of conglomerates, presumably due to the steric and electrostatic repulsion between fragments. This leads to greater interfragment spacing, where water can accommodate, and to

reduced intermolecular interactions. In contrast, nonglycosylated systems, after experiencing extension due to shear stress, establish conglomerates with reduced spacing available for water and pronounced intermolecular interactions. Note, however, that such systems eventually disperse in response to external shear stress. The strong shear-driven drop of viscosity in unglycosylated lubricin simulations is dampened upon glycosylation as they largely lack interchain interactions and thus are less affected in their structural ensemble by shear (Figure 6D). Interestingly, neither the elongation (Figure 6C) of the chains nor their alignment (Figure 7D,E) directly relates with the dampening. Overall, the lowering in viscosity by shear is suggested to be related to the amount of space between chains available to the solvent, a quantity that is promoted by the shear-dependent elongation and alignment of the (electrically charged) glycosylated chains. Enhanced lubrication has been observed for charged polymers and this enhancement has been attributed to steric repulsion and electrostatics too.^{93,94} Accordingly, our data support the notion that lubricin functions as a charged and tethered polymer brush,^{7,95} in which grafting glycans crucially modulate lubrication both by steric and electrostatic means. It is likely that other highly glycosylated systems such as mucin or aggrecan show a similar behavior when sheared.^{23,96,97}

We concentrated only on the central disordered region of lubricin. Consideration of the terminal domains and possible interactions between them was too computationally expensive at an atomistic resolution and was therefore beyond the scope of this study. In particular, disulfide bonds between the terminal domains, which mediate the formation of gel-like mucin networks,^{98,99} were not explicitly considered. However, in our simulations we considered multiple short fragments, spanning the whole lubricin's disordered mucin-like region, and we let them interact with each other in a confined volume. This situation could resemble, in a first approximation, the local interactions that take place between pieces of an entangled chain (or chains) whose ends are cross-linked by disulfide bonds. Accordingly, our simulations provide insightful information on the bulk rheological properties of conglomerates of disordered and glycosylated mucin-like lubricin chains, in potential coexistence with the solid-like disulfide-bonded network occurring at the terminal domains. How the interplay between the structured and disordered regions mediates the rheological function of lubricin remains to be elucidated. Computationally, coarse-graining approaches are a promising route.^{100–102}

Taking these observations together, multisite O-glycosylation affects the viscosity 2-fold: first, it renders the initial (zero shear) viscosity relatively low due to steric hindrance and electrostatic repulsion causing a reduction in interchain interactions, compared to a nonglycosylated lubricin system at the same mass density. Second, it lets the viscosity fall less dramatically at higher shear rates, maintaining values far above pure water. Lubricin solutions thus are “robustly viscous”, being able to nearly maintain their moderate viscosity over many orders of magnitude of shear rates, very different to their unglycosylated counterparts, which at drastic shear loads cannot uphold a significant resistance.

CONCLUSIONS

Our study aimed to investigate the impact of glycosylation on the structure and viscosity of lubricin, a vital protein involved in facilitating lubrication within synovial joints. Through

extensive MD simulations and continuum simulations we gained valuable insights into the role of O-glycans in influencing lubricin's properties.

Our findings reveal that glycosylated disordered lubricin solutions, on one hand, exhibit lower viscosities at zero shear, thus lowering friction, when compared to unglycosylated proteins at the same mass density. On the other hand, glycosylation attenuates the pronounced loss of viscosities with shear rates exhibited by their nonglycosylated counterparts. According to our results, the molecular basis of this effect is the presence of O-glycans, which promote the dispersion of lubricin, thereby preventing their clustering. Our continuum model showcases how quantitative viscosity relations from nanometer-scale molecular simulations can be harnessed to draw conclusions on much larger length scales and for more complex boundary conditions such as rugged cartilage surfaces sheared against each other. The insights from this work contribute to an understanding at the molecular level of how lubricin's conformational dynamics tailor its lubricating function in synovial joints.

ASSOCIATED CONTENT

Supporting Information

The Supporting Information is available free of charge at <https://pubs.acs.org/doi/10.1021/acs.biomac.3c01348>.

Intrinsic disorder of the middle region of lubricin, composition of O-glycans, distribution of glycosylated residues, total charge of glycosylated and nonglycosylated fragments of different peptides, and simulation details (PDF)

AUTHOR INFORMATION

Corresponding Authors

Camilo Aponte-Santamaría – Heidelberg Institute for Theoretical Studies, Heidelberg 69118, Germany;

orcid.org/0000-0002-8427-6965;

Email: camilo.aponte@h-its.org

Frauke Gräter – Heidelberg Institute for Theoretical Studies, Heidelberg 69118, Germany; University of Heidelberg, Heidelberg 69120, Germany; orcid.org/0000-0003-2891-3381; Email: frauke.graeter@h-its.org

Authors

Saber Boushehri – Heidelberg Institute for Theoretical Studies, Heidelberg 69118, Germany; University of Heidelberg, Heidelberg 69120, Germany; Karlsruhe Institute of Technology (KIT), Karlsruhe 76131, Germany

Hannes Holey – Karlsruhe Institute of Technology (KIT), Karlsruhe 76131, Germany; Department of Microsystems Engineering, University of Freiburg, Freiburg 79110, Germany

Matthias Brosz – Heidelberg Institute for Theoretical Studies, Heidelberg 69118, Germany; University of Heidelberg, Heidelberg 69120, Germany

Peter Gumbsch – Karlsruhe Institute of Technology (KIT), Karlsruhe 76131, Germany; Fraunhofer IWM, Freiburg 79108, Germany

Lars Pastewka – Department of Microsystems Engineering, University of Freiburg, Freiburg 79110, Germany

Complete contact information is available at: <https://pubs.acs.org/10.1021/acs.biomac.3c01348>

Notes

The authors declare no competing financial interest.

ACKNOWLEDGMENTS

We gratefully acknowledge support by the German Research Foundation (DFG) through the RTG/GRK-2450 graduate school program; the Klaus Tschira Foundation; and the state of Baden-Württemberg through bwHPC. Special thanks are extended to Isabel M Martin, Mohamed Tarek Elewa, and Nicholas Michelarakis for their insightful discussion.

REFERENCES

- (1) Vakis, A. I.; Yastrebov, V. A.; Scheibert, J.; Nicola, L.; Dini, D.; Minfray, C.; Almqvist, A.; Paggi, M.; Lee, S.; Limbert, G.; et al. Modeling and simulation in tribology across scales: An overview. *Tribol. Int.* **2018**, *125*, 169–199.
- (2) Klein, J. Molecular mechanisms of synovial joint lubrication. *Proc. Inst. Mech. Eng., Part J* **2006**, *220*, 691–710.
- (3) Jay, G. D.; Waller, K. A. The biology of lubricin: near frictionless joint motion. *Matrix Biol.* **2014**, *39*, 17–24.
- (4) Jahn, S.; Seror, J.; Klein, J. Lubrication of articular cartilage. *Annu. Rev. Biomed. Eng.* **2016**, *18*, 235–258.
- (5) Gonzales, G.; Zauscher, S.; Varghese, S. Progress in the design and synthesis of viscosupplements for articular joint lubrication. *Curr. Opin. Colloid Interface Sci.* **2023**, *66*, 101708.
- (6) Lee, Y.; Choi, J.; Hwang, N. S. Regulation of lubricin for functional cartilage tissue regeneration: a review. *Biomater. Res.* **2018**, *22*, 9.
- (7) Zappone, B.; Ruths, M.; Greene, G. W.; Jay, G. D.; Israelachvili, J. N. Adsorption, lubrication, and wear of lubricin on model surfaces: polymer brush-like behavior of a glycoprotein. *Biophys. J.* **2007**, *92*, 1693–1708.
- (8) Jones, A. R.; Gleghorn, J. P.; Hughes, C. E.; Fitz, L. J.; Zollner, R.; Wainwright, S. D.; Caterson, B.; Morris, E. A.; Bonassar, L. J.; Flannery, C. R. Binding and localization of recombinant lubricin to articular cartilage surfaces. *J. Orthop. Res.* **2007**, *25*, 283–292.
- (9) Flowers, S. A.; Zieba, A.; Örnros, J.; Jin, C.; Rolfson, O.; Björkman, L. I.; Eisler, T.; Kalamajski, S.; Kamali-Moghaddam, M.; Karlsson, N. G. Lubricin binds cartilage proteins, cartilage oligomeric matrix protein, fibronectin and collagen II at the cartilage surface. *Sci. Rep.* **2017**, *7*, 13149.
- (10) Greene, G. W.; Martin, L. L.; Tabor, R. F.; Michalczyk, A.; Ackland, L. M.; Horn, R. Lubricin: A versatile, biological anti-adhesive with properties comparable to polyethylene glycol. *Biomaterials* **2015**, *53*, 127–136.
- (11) Jumper, J.; Evans, R.; Pritzel, A.; Green, T.; Figurnov, M.; Ronneberger, O.; Tunyasuvunakool, K.; Bates, R.; Židek, A.; Potapenko, A.; et al. Highly accurate protein structure prediction with AlphaFold. *Nature* **2021**, *596*, 583–589.
- (12) Ishida, T.; Kinoshita, K. PrDOS: prediction of disordered protein regions from amino acid sequence. *Nucleic Acids Res.* **2007**, *35*, W460–W464.
- (13) Ali, L.; Flowers, S. A.; Jin, C.; Bennet, E. P.; Ekwall, A.-K. H.; Karlsson, N. G. The O-glycomap of lubricin, a novel mucin responsible for joint lubrication, identified by site-specific glycopeptide analysis. *Mol. Cell. Proteomics* **2014**, *13*, 3396–3409.
- (14) Garg, H. G.; Swann, D. A.; Glasgow, L. R. The structure of the O-glycosylated-linked oligosaccharide chains of LPG-I, a glycoprotein present in articular lubricating fraction of bovine synovial fluid. *Carbohydr. Res.* **1980**, *78*, 79–88.
- (15) Svala, E.; Jin, C.; Rüetschi, U.; Ekman, S.; Lindahl, A.; Karlsson, N.; Skjöldebrand, E. Characterisation of lubricin in synovial fluid from horses with osteoarthritis. *Equine Vet. J.* **2017**, *49*, 116–123.
- (16) Flowers, S. A.; Lane, C. S.; Karlsson, N. G. Deciphering isomers with a multiple reaction monitoring method for the complete detectable O-glycan repertoire of the candidate therapeutic, lubricin. *Anal. Chem.* **2019**, *91*, 9819–9827.
- (17) Zappone, B.; Greene, G. W.; Oroudjev, E.; Jay, G. D.; Israelachvili, J. N. Molecular aspects of boundary lubrication by human lubricin: effect of disulfide bonds and enzymatic digestion. *Langmuir* **2008**, *24*, 1495–1508.
- (18) Sun, Z.; Feeney, E.; Guan, Y.; Cook, S. G.; Gourdon, D.; Bonassar, L. J.; Putnam, D. Boundary mode lubrication of articular cartilage with a biomimetic diblock copolymer. *Proc. Natl. Acad. Sci. U.S.A.* **2019**, *116*, 12437–12441.
- (19) Sarkar, A.; Gul, K. Glycation influencing lubrication: Tribology principles derived from nature to inspire future food colloid design. *Curr. Opin. Colloid Interface Sci.* **2024**, *69*, 101782.
- (20) Crouzier, T.; Boettcher, K.; Geonnotti, A. R.; Kavanaugh, N. L.; Hirsch, J. B.; Ribbeck, K.; Lieleg, O. Modulating Mucin Hydration and Lubrication by Deglycosylation and Polyethylene Glycol Binding. *Adv. Mater. Interfaces* **2015**, *2*, 1500308.
- (21) Marczyński, M.; Balzer, B. N.; Jiang, K.; Lutz, T. M.; Crouzier, T.; Lieleg, O. Charged glycan residues critically contribute to the adsorption and lubricity of mucins. *Colloids Surf., B* **2020**, *187*, 110614.
- (22) Slomiany, B. L.; Sarosiek, J.; Slomiany, A. Role of carbohydrates in the viscosity and permeability of gastric mucin to hydrogen ion. *Biochem. Biophys. Res. Commun.* **1987**, *142*, 783–790.
- (23) Innes-Gold, S. N.; Berezney, J. P.; Saleh, O. A. Single-molecule stretching shows glycosylation sets tension in the hyaluronan-aggregan bottlebrush. *Biophys. J.* **2020**, *119*, 1351–1358.
- (24) Pradal, C.; Yakubov, G. E.; Williams, M. A.; McGuckin, M. A.; Stokes, J. R. Lubrication by biomacromolecules: mechanisms and biomimetic strategies. *Bioinspiration Biomimetics* **2019**, *14*, 051001.
- (25) Cai, Z.; Zhang, H.; Wei, Y.; Wu, M.; Fu, A. Shear-thinning hyaluronan-based fluid hydrogels to modulate viscoelastic properties of osteoarthritis synovial fluids. *Biomater. Sci.* **2019**, *7*, 3143–3157.
- (26) Bonnevie, E. D.; Galesso, D.; Secchieri, C.; Cohen, I.; Bonassar, L. J. Elastoviscous transitions of articular cartilage reveal a mechanism of synergy between lubricin and hyaluronic acid. *PLoS One* **2015**, *10*, No. e0143415.
- (27) Sultan, S.; Siqueira, G.; Zimmermann, T.; Mathew, A. P. 3D printing of nano-cellulosic biomaterials for medical applications. *Curr. Opin. Biomed. Eng.* **2017**, *2*, 29–34.
- (28) Cone, R. A. Barrier properties of mucus. *Adv. Drug Delivery Rev.* **2009**, *61*, 75–85.
- (29) Tazraei, P.; Riasi, A.; Takabi, B. The influence of the non-Newtonian properties of blood on blood-hammer through the posterior cerebral artery. *Math. Biosci.* **2015**, *264*, 119–127.
- (30) Michelarakis, N.; Franz, F.; Gkagkas, K.; Gräter, F. Longitudinal strand ordering leads to shear thinning in Nafion. *Phys. Chem. Chem. Phys.* **2021**, *23*, 25901–25910.
- (31) Malkin, A. Y. Non-Newtonian viscosity in steady-state shear flows. *J. Non-Newtonian Fluid Mech.* **2013**, *192*, 48–65.
- (32) Zgorski, A.; Pastor, R. W.; Lyman, E. Surface shear viscosity and interleaflet friction from nonequilibrium simulations of lipid bilayers. *J. Chem. Theory Comput.* **2019**, *15*, 6471–6481.
- (33) Dingcheng, X.; Yipan, D.; Zhenyao, W.; Tianhao, L.; Yinshui, L. Viscosity evolution of water glycol in deep-sea environment at high pressure and low temperature. *J. Mol. Liq.* **2023**, *387*, 122387.
- (34) Ewen, J.; Heyes, D.; Dini, D. Advances in nonequilibrium molecular dynamics simulations of lubricants and additives. *Friction* **2018**, *6*, 349–386.
- (35) Savio, D.; Pastewka, L.; Gumbsch, P. Boundary lubrication of heterogeneous surfaces and the onset of cavitation in frictional contacts. *Sci. Adv.* **2016**, *2*, No. e1501585.
- (36) Mohamed, K. M.; Mohamad, A. A review of the development of hybrid atomistic–continuum methods for dense fluids. *Microfluid. Nanofluidics* **2010**, *8*, 283–302.
- (37) Khare, R.; De Pablo, J.; Yethiraj, A. Molecular simulation and continuum mechanics study of simple fluids in non-isothermal planar Couette flows. *J. Chem. Phys.* **1997**, *107*, 2589–2596.
- (38) Zerze, G. H.; Mittal, J. Effect of O-linked glycosylation on the equilibrium structural ensemble of intrinsically disordered polypeptides. *J. Phys. Chem. B* **2015**, *119*, 15583–15592.

- (39) Beckham, G. T.; Bomble, Y. J.; Matthews, J. F.; Taylor, C. B.; Resch, M. G.; Yarbrough, J. M.; Decker, S. R.; Bu, L.; Zhao, X.; McCabe, C.; et al. The O-glycosylated linker from the *Trichoderma reesei* Family 7 cellulase is a flexible, disordered protein. *Biophys. J.* **2010**, *99*, 3773–3781.
- (40) Shakibi, S.; Onck, P. R.; Van der Giessen, E. A One-Bead-Per-Saccharide (IBPS) Model for Glycosaminoglycans. *J. Chem. Theory Comput.* **2023**, *19*, 5491–5502.
- (41) Hess, B. Determining the shear viscosity of model liquids from molecular dynamics simulations. *J. Chem. Phys.* **2002**, *116*, 209–217.
- (42) Balasubramanian, S.; Mundy, C. J.; Klein, M. L. Shear viscosity of polar fluids: Molecular dynamics calculations of water. *J. Chem. Phys.* **1996**, *105*, 11190–11195.
- (43) Reynolds, O. On the Theory of Lubrication and Its Application to Mr. Beauchamp Tower's Experiments, Including an Experimental Determination of the Viscosity of Olive Oil. *Philos. Trans. R. Soc. London* **1886**, *177*, 157–234.
- (44) Carreau, P. J. Rheological Equations from Molecular Network Theories. *Trans. Soc. Rheol.* **1972**, *16*, 99–127.
- (45) Jin, F.; Gräter, F. How multisite phosphorylation impacts the conformations of intrinsically disordered proteins. *PLoS Comput. Biol.* **2021**, *17*, No. e1008939.
- (46) Martin, I. M.; Aponte-Santamaría, C.; Schmidt, L.; Hedtfeld, M.; Iusupov, A.; Musacchio, A.; Gräter, F. Phosphorylation tunes elongation propensity and cohesiveness of INCENP's intrinsically disordered region. *J. Mol. Biol.* **2022**, *434*, 167387.
- (47) Hanwell, M. D.; Curtis, D. E.; Lonie, D. C.; Vandermeersch, T.; Zurek, E.; Hutchison, G. R. Avogadro: an advanced semantic chemical editor, visualization, and analysis platform. *J. Cheminf.* **2012**, *4*, 17.
- (48) Abraham, M. J.; Murtola, T.; Schulz, R.; Páll, S.; Smith, J. C.; Hess, B.; Lindahl, E. GROMACS: High performance molecular simulations through multi-level parallelism from laptops to supercomputers. *SoftwareX* **2015**, *1–2*, 19–25.
- (49) Best, R. B.; Hummer, G. Optimized molecular dynamics force fields applied to the helix-coil transition of polypeptides. *J. Phys. Chem. B* **2009**, *113*, 9004–9015.
- (50) Aliev, A. E.; Kulke, M.; Khaneja, H. S.; Chudasama, V.; Sheppard, T. D.; Lanigan, R. M. Motional timescale predictions by molecular dynamics simulations: case study using proline and hydroxyproline sidechain dynamics. *Proteins: Struct., Funct., Bioinf.* **2014**, *82*, 195–215.
- (51) Kirschner, K. N.; Yongye, A. B.; Tschampel, S. M.; González-Outeiriño, J.; Daniels, C. R.; Foley, B. L.; Woods, R. J. GLYCAM06: a generalizable biomolecular force field. *Carbohydrates. J. Comput. Chem.* **2008**, *29*, 622–655.
- (52) Bernardi, A.; Faller, R.; Reith, D.; Kirschner, K. N. ACPYPE update for nonuniform 1–4 scale factors: Conversion of the GLYCAM06 force field from AMBER to GROMACS. *SoftwareX* **2019**, *10*, 100241.
- (53) Sousa da Silva, A. W.; Vranken, W. F. ACPYPE-Antechamber python parser interface. *BMC Res. Notes* **2012**, *5*, 367–368.
- (54) Piana, S.; Donchev, A. G.; Robustelli, P.; Shaw, D. E. Water dispersion interactions strongly influence simulated structural properties of disordered protein states. *J. Phys. Chem. B* **2015**, *119*, 5113–5123.
- (55) Bussi, G.; Donadio, D.; Parrinello, M. Canonical sampling through velocity rescaling. *J. Chem. Phys.* **2007**, *126*, 014101.
- (56) Parrinello, M.; Rahman, A. Polymorphic transitions in single crystals: A new molecular dynamics method. *J. Appl. Phys.* **1981**, *52*, 7182–7190.
- (57) Darden, T.; York, D.; Pedersen, L. Particle mesh Ewald: An $n \log(n)$ method for Ewald sums in large systems. *J. Chem. Phys.* **1993**, *98*, 10089–10092.
- (58) Hess, B. P-LINCS: A parallel linear constraint solver for molecular simulation. *J. Chem. Theory Comput.* **2008**, *4*, 116–122.
- (59) Green, M. S. Markoff Random Processes and the Statistical Mechanics of Time-dependent Phenomena. II. Irreversible Processes in Fluids. *J. Chem. Phys.* **1954**, *22*, 398–413.
- (60) Kubo, R. Statistical-Mechanical Theory of Irreversible Processes. I. General Theory and Simple Applications to Magnetic and Conduction Problems. *J. Phys. Soc. Jpn.* **1957**, *12*, 570–586.
- (61) Zhang, Y.; Otani, A.; Maginn, E. J. Reliable viscosity calculation from equilibrium molecular dynamics simulations: A time decomposition method. *J. Chem. Theory Comput.* **2015**, *11*, 3537–3546.
- (62) von Bülow, S.; Siggel, M.; Linke, M.; Hummer, G. Dynamic cluster formation determines viscosity and diffusion in dense protein solutions. *Proc. Natl. Acad. Sci. U.S.A.* **2019**, *116*, 9843–9852.
- (63) Prass, T. M.; Garidel, P.; Blech, M.; Schäfer, L. V. Viscosity Prediction of High-Concentration Antibody Solutions with Atomistic Simulations. *J. Chem. Inf. Model.* **2023**, *63*, 6129–6140.
- (64) Mathas, D.; Holweger, W.; Wolf, M.; Bohnert, C.; Bakolas, V.; Procelewaska, J.; Wang, L.; Bair, S.; Skylaris, C.-K. Evaluation of methods for viscosity simulations of lubricants at different temperatures and pressures: a case study on PAO-2. *Tribol. Trans.* **2021**, *64*, 1138–1148.
- (65) Maginn, E. J.; Messerly, R. A.; Carlson, D. J.; Roe, D. R.; Elliot, J. R. Best practices for computing transport properties I. Self-diffusivity and viscosity from equilibrium molecular dynamics [article v1.0]. *Living J. Comput. Mol. Sci.* **2019**, *1*, 6324.
- (66) Todd, B. D.; Daivis, P. J. *Nonequilibrium Molecular Dynamics: Theory, Algorithms and Applications*; Cambridge University Press, 2017.
- (67) Lees, A.; Edwards, S. The computer study of transport processes under extreme conditions. *J. Phys. C: Solid State Phys.* **1972**, *5*, 1921–1928.
- (68) Bindgen, S.; Weik, F.; Weeber, R.; Koos, E.; de Buyl, P. Lees–Edwards boundary conditions for translation invariant shear flow: Implementation and transport properties. *Phys. Fluids* **2021**, *33*, 083615.
- (69) Hess, B. Improve the deform option. https://gitlab.com/gromacs/gromacs/-/merge_requests/3141 (accessed Sep 26, 2022).
- (70) Amaya-Espinosa, H.; Alexander-Katz, A.; Aponte-Santamaría, C. The interplay between adsorption and aggregation of von Willebrand factor chains in shear flows. *Biophys. J.* **2023**, *122*, 3831–3842.
- (71) Brosz, M.; Michelarakis, N.; Bunz, U. H.; Aponte-Santamaría, C.; Gräter, F. Martini 3 coarse-grained force field for poly (paraphenylene ethynylene) s. *Phys. Chem. Chem. Phys.* **2022**, *24*, 9998–10010.
- (72) Humphrey, W.; Dalke, A.; Schulten, K. VMD: visual molecular dynamics. *J. Mol. Graph.* **1996**, *14*, 33–38.
- (73) Jakobsson, B.; Floberg, L. *The Finite Journal Bearing, Considering Vaporization: (Das Gleitlager von endlicher Breite mit Verdampfung)*, Chalmers Tekniska Högskolas Handlingar 190, 1957.
- (74) Olsson, K.-O. *Cavitation in Dynamically Loaded Bearings*, Transactions of Chalmers University of Technology 308, 1965.
- (75) Woloszynski, T.; Podsiadlo, P.; Stachowiak, G. W. Efficient Solution to the Cavitation Problem in Hydrodynamic Lubrication. *Tribol. Lett.* **2015**, *58*, 18.
- (76) Almqvist, A.; Burtseva, E.; Rajagopal, K.; Wall, P. On Flow of Power-Law Fluids between Adjacent Surfaces: Why Is It Possible to Derive a Reynolds-type Equation for Pressure-Driven Flow, but Not for Shear-Driven Flow? *Appl. Eng. Sci.* **2023**, *15*, 100145.
- (77) Cross, M. M. Rheology of Non-Newtonian Fluids: A New Flow Equation for Pseudoplastic Systems. *J. Colloid Sci.* **1965**, *20*, 417–437.
- (78) Dowson, D. A Generalized Reynolds Equation for Fluid-Film Lubrication. *Int. J. Mech. Sci.* **1962**, *4*, 159–170.
- (79) Kohn, J. E.; Millett, I. S.; Jacob, J.; Zagrovic, B.; Dillon, T. M.; Cingel, N.; Dothager, R. S.; Seifert, S.; Thiyagarajan, P.; Sosnick, T. R.; et al. Random-coil behavior and the dimensions of chemically unfolded proteins. *Proc. Natl. Acad. Sci. U.S.A.* **2004**, *101*, 12491–12496.
- (80) Morozova, T. I.; García, N. A.; Barrat, J.-L. Temperature dependence of thermodynamic, dynamical, and dielectric properties of water models. *J. Chem. Phys.* **2022**, *156*, 126101.
- (81) Newcombe, E. A.; Delaforge, E.; Hartmann-Petersen, R.; Skriver, K.; Kragelund, B. B. How phosphorylation impacts intrinsi-

- cally disordered proteins and their function. *Essays Biochem.* **2022**, *66*, 901–913.
- (82) Owen, I.; Shewmaker, F. The role of post-translational modifications in the phase transitions of intrinsically disordered proteins. *Int. J. Mol. Sci.* **2019**, *20*, 5501.
- (83) Brito, A.; Dave, D.; Lampel, A.; Castro, V. I.; Kroiss, D.; Reis, R. L.; Tuttle, T.; Ulijn, R. V.; Pires, R. A.; Pashkuleva, I. Expanding the conformational landscape of minimalistic tripeptides by their O-glycosylation. *J. Am. Chem. Soc.* **2021**, *143*, 19703–19710.
- (84) Kestin, J.; Sokolov, M.; Wakeham, W. A. Viscosity of liquid water in the range $-8\text{ }^{\circ}\text{C}$ to $150\text{ }^{\circ}\text{C}$. *J. Phys. Chem. Ref. Data* **1978**, *7*, 941–948.
- (85) Ludwig, T. E.; Cowman, M. K.; Jay, G. D.; Schmidt, T. A. Effects of concentration and structure on proteoglycan 4 rheology and interaction with hyaluronan. *Biorheology* **2015**, *51*, 409–422.
- (86) Zwanzig, R. Time-correlation functions and transport coefficients in statistical mechanics. *Annu. Rev. Phys. Chem.* **1965**, *16*, 67–102.
- (87) Kuhnhold, A.; Paul, W. Passive one-particle microrheology of an unentangled polymer melt studied by molecular dynamics simulation. *Phys. Rev. E: Stat., Nonlinear, Soft Matter Phys.* **2014**, *90*, 022602.
- (88) Putignano, C.; Burris, D.; Moore, A.; Dini, D. Cartilage Rehydration: The Sliding-Induced Hydrodynamic Triggering Mechanism. *Acta Biomater.* **2021**, *125*, 90–99.
- (89) Codrignani, A.; Peeters, S.; Holey, H.; Stief, F.; Savio, D.; Pastewka, L.; Moras, G.; Falk, K.; Moseler, M. Toward a continuum description of lubrication in highly pressurized nanometer-wide constrictions: The importance of accurate slip laws. *Sci. Adv.* **2023**, *9*, No. eadi2649.
- (90) Simou, K.; Jones, S. W.; Davis, E. T.; Preece, J.; Zhang, Z. J. Rheological and interface adhesive properties of osteoarthritic synovial fluids. *Biotribology* **2022**, *32*, 100227.
- (91) Elsaid, K.; Fleming, B.; Oksendahl, H.; Machan, J.; Fadale, P.; Hulstyn, M.; Shalvoy, R.; Jay, G. Decreased lubricin concentrations and markers of joint inflammation in the synovial fluid of patients with anterior cruciate ligament injury. *Arthritis Rheum.* **2008**, *58*, 1707–1715.
- (92) Estrella, R. P.; Whitelock, J. M.; Packer, N. H.; Karlsson, N. G. The glycosylation of human synovial lubricin: implications for its role in inflammation. *Biochem. J.* **2010**, *429*, 359–367.
- (93) Pincus, P. Colloid stabilization with grafted polyelectrolytes. *Macromolecules* **1991**, *24*, 2912–2919.
- (94) Raviv, U.; Giasson, S.; Kampf, N.; Gohy, J.-F.; Jérôme, R.; Klein, J. Lubrication by charged polymers. *Nature* **2003**, *425*, 163–165.
- (95) Daniel, M. Boundary cartilage lubrication: Review of current concepts. *Wien Med. Wochenschr.* **2014**, *164*, 88–94.
- (96) Lai, S. K.; Wang, Y.-Y.; Wirtz, D.; Hanes, J. Micro-and macrorheology of mucus. *Adv. Drug Delivery Rev.* **2009**, *61*, 86–100.
- (97) Chandran, P. L.; Horkay, F. Aggrecan, an unusual polyelectrolyte: review of solution behavior and physiological implications. *Acta Biomater.* **2012**, *8*, 3–12.
- (98) Abubacker, S.; Ponjevic, D.; Ham, H. O.; Messersmith, P. B.; Matyas, J. R.; Schmidt, T. A. Effect of disulfide bonding and multimerization on proteoglycan 4's cartilage boundary lubricating ability and adsorption. *Connect. Tissue Res.* **2016**, *57*, 113–123.
- (99) Flowers, S.; Kalamajski, S.; Ali, L.; Björkman, L.; Raj, J.; Asperg, A.; Karlsson, N.; Jin, C. Cartilage oligomeric matrix protein forms protein complexes with synovial lubricin via non-covalent and covalent interactions. *Osteoarthritis Cartilage* **2017**, *25*, 1496–1504.
- (100) Souza, P. C.; Alessandri, R.; Barnoud, J.; Thallmair, S.; Faustino, I.; Grünewald, F.; Patmanidis, I.; Abdizadeh, H.; Bruininks, B. M.; Wassenaar, T. A.; et al. Martini 3: a general purpose force field for coarse-grained molecular dynamics. *Nat. Methods* **2021**, *18*, 382–388.
- (101) Thomasen, F. E.; Skaalum, T.; Kumar, A.; Srinivasan, S.; Vanni, S.; Lindorff-Larsen, K. Rescaling protein-protein interactions improves Martini 3 for flexible proteins in solution. **2023**, bioRxiv. 10.1101/2023.05.29.542689.
- (102) Grünewald, F.; Punt, M. H.; Jefferys, E. E.; Vainikka, P. A.; König, M.; Virtanen, V.; Meyer, T. A.; Pezeshkian, W.; Gormley, A. J.; Karonen, M.; et al. Martini 3 coarse-grained force field for carbohydrates. *J. Chem. Theory Comput.* **2022**, *18*, 7555–7569.